Development of trivalent europium-doped oxide phosphors
(3 価のユーロピウムをドープした酸化物系蛍光体の開発研究)

2016 年

Kang Yipu

TABLE OF CONTENTS

CHAPTER 1: Introduction

1.1. General background of phosphors

The phosphor was first invented in the early 17^{th} century called "Bolognian stone" ($BaSO_4$), which was the annealed product being BaS known as a host materials for phosphor. After the discovery of the BaS, same findings were reported from many places in the world and these species of light emitting stones were named "phosphors" [1].

Nowadays, the phosphor believed as a substance that exhibits the phenomenon of luminescence. Depending on the excitation source, the luminescence can be classified into photoluminescence (PL), cathodoluminescence (CL) and electroluminescence (EL). Additionally, depending on the lifetime (τ) of the phosphors, the luminescence can be classified as the fluorescence ($\tau \leq 0.01$ s) and the phosphorescence ($\tau \geq 0.1$ s).

There are two kinds of luminescence mechanisms: first is the luminescence from the semiconductor; second is the luminescence from the localized center. It is well known that when semiconductors are doped with impurities, the lattices of the semiconductors are distorted and the energy level structures of the semiconductors are also affected, and due to the spontaneous recombination of electronic excitations, the semiconductor phosphor produces a flux of spontaneously emitted light (e. g., donor-accepter pair luminescence in $ZnS:Ag^{+}$, Cl-).

On the other hand, in the case of the luminescence from the localized center, the absorption and emission spectra of simple activator centers are related to the activator atoms. For example, when a phosphor is activated by ions of rare earth elements, the spectra of the luminescent centers turn out to be line spectra produced by quantum transitions in the inner electron shells of the ions. The effect of the lattice shifting and splitting of the spectral lines by the crystal filed, for example, the stark effect and in the superposition of additional frequencies correspond to lattice vibrations. When a phosphor is activated by atoms of elements, whose spectra are shown by transitions in an outer electron shell, the lattice causes the spectral lines to be broadened into band.

1.2. Excitation method

The various types of luminescence are shown in Table 1-1. Photoluminescence occurs after excitation with light (radiation within the optical range). The luminescence can be also produced under excitation with an electron beam, and in this case it is called cathodoluminescence. This technique is traditionally used to investigate some characteristics of samples, such as trace lattice defects and impurities, as well as investigate crystal distortion. Excitation by high energy electromagnetic radiation such as α-rays (helium nuclei), X-ray, β-rays (electrons), or γ-rays leads to a kind of photoluminescence called radioluminescence. On the other hand, the thermoluminescence happens when a substance emits light as a result of the release of energy stored in traps by thermal heating. This mechanism is different from the radiation from the heated blackbody. Electroluminescence occurs as a result of energy transition by an electric current through a phosphor material, as in nightlight panels. Triboluminescence is the emission of light by a mechanical disturbance, such as the light that emerges when some disturbed tapes are unrolled. Acoustic waves passing through a liquid can lead to the sonoluminescence. Chemiluminescence is the result of chemical reactions inside an organic material. Bioluminescence is the main source of light in the deep ocean [2].

Table 1-1. The various types of luminescence.

Name	Excitation mechanism
Photoluminescence	Light
Cathodoluminescence	Electrons
Radioluminescence	X-rays, α-rays, β-rays, or γ-rays
Thermoluminescence	Heating
Electroluminescence	Electric field or current
Triboluminescence	Mechanical energy
Sonoluminescence	Sound waves in liquids
Chemiluminescence and bioluminescence	Chemical reactions

1.3. Energy transfer methods

In the phosphor, there are two kinds of energy transfer method: energy transition with a band to band model [3] and the energy transition with a localized model [4].

Energy transition with a band to band model: in the solid state physics, the electronic band structure of a solid explain the ranges of energy, which an electron within the solid may have and ranges of energy that it may not have. In a semiconductor, the band structure surrounding with the Fermi level, has been believed as the band gap [5]. The closest band above the band gap is called the conduction band, and the closest band under the band gap is called the valence band. Normally, when the semiconductors are irradiated by the light, the transmission, reflection and absorption will occur. Normally, the absorption of the light will create the lattice excitation or electronic excitation in the semiconductor and the electrons are excited to the higher states. Then, the excited electrons will come back to the original states after release the excitation energy in the form of lattice vibrations or light emission.

Energy transition with a localized model: when considering optical absorption or emission within a single ion or a group of ions in a solid, it is normally to treat as an optical transition with a localized model [6]. Usually, most of the phosphors have localized luminescent centers and contain a large variety of ions more than delocalized centers. Normally, the lanthanide based luminescence belongs to the energy transition with a localized model.

1.4. Lanthanide based luminescence

The photoluminescence properties of the rare earth (lanthanide)-based phosphors have been attracted so many interesting of the researchers for several years [7]. Because of the narrow emission bandwidths, large Stokes shifts and long fluorescence lifetimes, the lanthanide-based phosphors have been used in different kinds of fields [8]. The trivalent ions of the rare earth series have been used as the localized ions in the phosphor, and the properties of these ions depend on the gradual filling of the 4f

orbitals which from La^{3+} ($_4f^0$) to Lu^{3+} ($_4f^{14}$) as shows in Table 1-2 [8].

Table 1-2. Electronic structure of the trivalent Lanthanide ions.

element	symbol	atomic number (Z)	configuration Ln^{3+}	ground state Ln^{3+}
lanthanum	La	57	[Xe]	$^1S_0$
cerium	Ce	58	[Xe]$4f^1$	$^2F_{5/2}$
praseodymium	Pr	59	[Xe]$4f^2$	$^3H_4$
neodymium	Nd	60	[Xe]$4f^3$	$^4I_{9/2}$
promethium	*Pm*	61	[Xe]$4f^4$	$^5I_4$
samarium	Sm	62	[Xe]$4f^5$	$^6H_{5/2}$
europium	Eu	63	[Xe]$4f^6$	$^7F_0$
gadolinium	Gd	64	[Xe]$4f^7$	$^8S_{7/2}$
terbium	Tb	65	[Xe]$4f^8$	$^7F_6$
dysprosium	Dy	66	[Xe]$4f^9$	$^6H_{15/2}$
holmium	Ho	67	[Xe]$4f^{10}$	$^5I_8$
erbium	Er	68	[Xe]$4f^{11}$	$^4I_{15/2}$
thulium	Tm	69	[Xe]$4f^{12}$	$^3H_6$
ytterbium	Yb	70	[Xe]$4f^{13}$	$^2F_{7/2}$
lutetium	Lu	71	[Xe]$4f^{14}$	$^1S_0$

Until now, it is well known that so many rare earth ions can show the very high color purity light emitting due to the f-f transitions from the inside 4f shell [9]. Depending on the basic color theory, the primary colors are red, green and blue, and other colors are composed of these three primary colors. For the trivalent rare earth ions, the Eu^{3+} shows the red color, Tb^{3+} shows the green color and the Tm^{3+} shows the blue color [10]. Except for these primary colors, Sm^{3+} shows the orange light; Er^{3+}, Yb^{3+} and Nd^{3+} show the luminescence property in the near infrared range, and the Gd^{3+} without organic ligands can exhibit the light in the ultraviolet region.

1.5. Host materials for the rare earth ions

In the rare earth ions (Ln^{3+}) doped inorganic materials, the matched host lattices can give a suitable and stable environment for the Ln^{3+} emitter. Because of the higher absorption coefficient than the Ln^{3+} emitter, the host materials have been used as an

effective energy absorber and transfer to the rare earth ions. The Ln^{3+} emitter doped in the host materials exhibits luminescence emissions from ultraviolet to the infrared light region under the excitation [11]. Only for the one kind of rare earth ions Eu^{3+}, several kinds of inorganic host materials like VO_4 [12], LaF_3 [13], $NaYF_4$ [14], Y_2O_3 [15] and Gd_2O_2S [16] can be used as the host materials. For example, due to the high efficient energy transfer from VO_4^{3-} groups to the Eu^{3+} ions, the Eu^{3+} doped YVO_4 phosphor shows a strong red luminescence. However, each kind of host materials has its own problems. Because of the high efficient energy transfer, Eu^{3+} doped Gd_2O_2S red phosphor has been commercially available. However, during long term utilization, such red color sulfide phosphors will degrade under electron beams. On the other hand, the rare earth oxides are excellent phosphor host materials that can offer long fluorescence lifetimes, narrow emission bandwidths and large Stokes shifts. Especially, among the rare earth oxides, cubic phase Gd_2O_3 is an excellent host material because of its good thermal stability, low phonon energy, chemical durability and the crystal lattice matched with all kinds of the rare earth ions.

1.6. Application of the phosphors

The applications of phosphors can be classified as following: fluorescent lamps, light emitting diodes (LEDs) and the vacuum fluorescent displays (VFDs).

Fluorescent lamp phosphors convert the ultraviolet emission of a rare-gas/mercury discharge plasma into visible light. In the 1940s, $Ca_5(PO_4)_3$(F, Cl):(Sb, Mn) was developed and came into use as the fluorescent phosphor [17]. This phosphor has two dominant emission bands, one is the blue band peaked near 480 nm due to the activator Sb^{3+} ions which absorb the 254 nm radiation of the discharge and emit a part of this energy in the blue band. The excitation energy is also transferred from Sb^{3+} to Mn^{2+} which resulting in the orange-red Mn^{2+} emission band peaked at around 580 nm. The blue/orange-red emission ban intensity ratio can be adjusted by controlling the relative amount of Mn^{2+} to Sb^{3+}. A further variation in color can be

achieved by changing the F/Cl ratio. However, the energy efficiency was as low as 75 lm/W.

During the 1970s, low pressure mercury fluorescent lamps were developed and the better color rendering property and higher efficiency were achieved. In the mid-1970s such fluorescent lamps were commercially available and contained blend of three rare earth-activated phosphors (namely tricolor or tri-phosphor blends): $Y_2O_3:Eu^{3+}$ (red), $MgAl_{11}O_{19}$: (Ce^{3+}, Tb^{3+}) (green) and $BaMgAl_{10}O_{17}:Eu^{2+}$ (blue).

The $Y_2O_3:Eu^{3+}$ phosphor absorbs the 254 nm mercury discharge emission through a charge transfer transition from O^{2-} to Eu^{3+}, and exhibits a red emission with a dominant peak at 611 nm corresponding to the electric dipole transition $^5D_0$ -$^7F_2$. The $MgAl_{11}O_{19}:Ce^{3+}$ is an efficient ultraviolet emitter under the excitation at 254 nm, which is due to the 4*f* and 5*d* transition in the Ce^{3+}. The doped-Tb^{3+} in $MgAl_{11}O_{19}:Ce^{3+}$ quenches the Ce^{3+} emission and generates the Tb^{3+} green emission as a result of the energy transfer from Ce^{3+} to Tb^{3+}. The $BaMgAl_{10}O_{17}:Eu^{2+}$ absorbs the UV light due to the allowed $4f^7 5d$ - $4f^6 5d^1$ transitions and exhibits the high intensity blue emission at 450 nm ascribed to the 4f-5d transition in the Eu^{2+}.

Recently, there is an increasing concern that environmentally hazardous mercury, which is central to the operation of fluorescent lamps. Thus a significant effort has been made to develop mercury-free lighting devices, and LEDs have been successfully put in use as the backlight sources, display screen, electronic equipment and general lighting, and currently white color LEDs are getting to be very popular. In addition to the lower environmental load, the LEDs have several advantages such as high energy efficiency, long lifetime. The Excellent color rendering property of the white LEDs has been also achieved by the combination of the GaN blue LED chip with green phosphors such as -SiAlON:Eu^{2+} and red phosphors like sulfide (Ca,Sr)S:Eu^{3+} and oxysulfide $Y_2O_2S:Eu^{3+}$.

On the other hand, in 1959, the first VFD device was developed by the Philips. Then in 1962, the Japanese company, Ise Denshi Kogyo Co. (now Noritake Itron Co.) created the first multi-segment VFD. Compared with the liquid crystal displays, the VFD exhibits a higher emitting intensity and higher contrast by using multiple color

phosphors such as $(Zn_{0.22}Cd_{0.78})S:Ag$ and $Gd_2O_2S:Eu^{3+}$ for red, ZnO:Zn and ZnS:Cu,Al for green, and ZnS:Ag and $ZnGa_2O_4$ for blue emissions [18].

1.7. Objectives of present study

There is continuing interest in phosphors with properties such as sufficient brightness, fast response and long term stability for use in modern luminescence devices. As mentioned in the previous section, the commercial red phosphors currently used for white LEDs and VFDs are $(Ca,Sr)S:Eu^{3+}$, $(Zn_{0.22}Cd_{0.78})S:Ag$, $Y_2O_2S:Eu^{3+}$ and $Gd_2O_2S:Eu^{3+}$. However, such sulfide and oxysulfide phosphors are moisture-sensitive, giving a poor chemical stability, which restricts long term utilization. Degradation also occurred under the electron beam excitation in vacuum. Therefore, it is important to develop novel environmentally friendly red-emitting phosphors that can be excited efficiently under UV or near-UV irradiation for white LEDs, and under low acceleration electron beam voltage for VFDs.

In this study, Eu^{3+} was selected as an efficient activator for red emission, while both rare earth oxide and oxide semiconductor were selected as stable and environmentally benign host materials. Especially, we focused on Gd_2O_3 and $SrIn_2O_4$. The useful phase of Gd_2O_3 as the host is cubic, and its crystal lattice is quite similar to that of cubic Eu_2O_3. On the other hand, $SrIn_2O_4$ with a reported bandgap of 3.6 eV, and has a strong absorption band at 396 nm, which perfectly matches with the emission spectrum of GaN-based LED chips.

The objective of present study is enhancing the red emission intensity of Eu^{3+}-doped Gd_2O_3 ($Gd_{2-x}Eu_xO_3$) and Eu^{3+}-doped $SrIn_2O_4$ ($SrIn_2O_4:Eu^{3+}$) for their practical use in LEDs and/or VFDs, and the effect of the second dopant on the red emission intensity as well as optimizing the amount of Eu^{3+} doped in the two different host lattice were systematically studied.

In Chapter 2, cubic $Gd_{1.88}Eu_{0.12}O_3$ powders were synthesized by the solid state reaction method at 1200 ℃, and the effect of Li^+-doping on their PL properties was

investigated and discussed. Effect of the Li^{+}-doping on and thermal stability of cubic $Gd_{1.88}Eu_{0.12}O_3$ was also discuss form a viewpoint of high-temperature application exceeding the cubic/monoclinic phase transformation temperature of 1250 ℃.

In Chapter 3, Li^{+}-doped $Gd_{1.88}Eu_{0.12}O_3$ phosphors were synthesized at 1200 ^{o}C in air by co-precipitation (CP) and solid solution (SS) methods. The PL and CL properties of the synthesized phosphors were studied and discussed based on the material factors in terms of the average crystallite size, dispersion property of Eu^{3+} ions in the host Gd_2O_3 and specific surface area of the phosphors.

In Chapter 4, $SrIn_2O_4$:Eu^{3+} phosphors were synthesized by the solid solution method at 1400 ℃ in air. The Eu^{3+} substitutions at the two different crystallographic In^{3+} sites and Sr^{2+} site were studied by the X-ray diffraction analysis combined with PL spectroscopic analysis. Then, to enhance the red PL emission intensity, optimization of the total amount of Eu^{3+} doped in the host $SrIn_2O_4$ was performed. Moreover, thermal quenching property at the usual LED's operating temperatures was studied and discussed.

References

[1] S. Shionoya, “Introduction of the handbook,” pp. 1-2 in Phosphor Handbook, edited by W. Yen, S. Shinoyama, H. Yamamoto (CRC Press, Boca Raton), 1998.

[2] J. Garcia Sole, L.E. Bausa, D. Jaque, An Introduction to the Optical Spectroscopy of Inorganic Solids, Chapter 1. 2005.

[3] Y. Galperin, Introduction to modern solid state physics, Chapter 5, 451-458.

[4] Q. Li, S. Xu, M. Xie, S. Tong, Europhysics, 71 (2005) 994.

[5] C. Kittel, Introduction to solid state physics, Chapter 9, 221-252.

[6] H. Jiang, R. Gomez-Abal, P. Rinke and M. Scheffler, Phy. Rev. Lett., 102 (2009) 126403.

[7] R. Bazzi, M. Flores-Gonzalez, C. Louis, K. Lebbou, C. Dujardin, A. Brenier, W. Zhang, O. Tillement, E. Bernstein and P. Perriat, J. Lumin., 102 (2003) 445.

[8] K. Binnemans, Chem. Rev., 109 (2009) 4283.

[9] L. Liu and X. Chen, Nanotechnology, 18 (2007) 255704.

[10] S. Gai, P. Yang, D. Wang, C. Li, N. Niu, F. He and X. Li, CrystEngComm, 13 (2011) 5480.

[11] S. Gai, C. Li, P. Yang and J. Lin, Chemical reviews, 114 (2014) 2343.

[12] Z. Xu, X. Kang, C. Li, Z. Hou, C. Zhang, D. Yang, G. Li, Y. Dai and J. Lin, J. Inorg. Chem., 14 (2010) 6706.

[13] A. Cross, S. May, F. Veggel and M. Berry, J. Phys. Chem. C, 114 (2010) 14740.

[14] C. Li, C. Zhang, Z. Hou, L. Wang, Z. Quan, H. Lian and J. Lin, J. Phys. Chem. C, 113 (2009) 2332.

[15] R. Si, Y. Zhang, H. Zhou, L. Sun and C. Yan, Chem. Mater., 19 (2007) 18.

[16] Y. Song, H. You, Y. Huang, M. Yang, Y. Zheng, L. Zhang and N. Guo, Inorg. Chem., 49 (2010) 11499.

[17] C. R. Ronda, T. Justel, H. Nikol, Journal of Alloys and Compounds, 275 (1998) 669.

[18] M. Baldo, M. Thompson and S. Forrest, Nature, 403 (1999) 750.

CHAPTER 2: Effect of lithium ion doping on cubic $Gd_{1.88}Eu_{0.12}O_3$: Enhancement of photoluminescence and thermal stability

2.1. Introduction

There is continuing interest in phosphors with properties such as sufficient brightness, fast response and long term stability for use in modern luminescence devices [1]. The most popular commercial materials currently used for red emission are sulfide phosphors such as $Zn_{0.2}Cd_{0.8}S:Ag^+$ and $Y_2O_2S:Eu^{3+}$ [2]. However, during long-term utilization, such sulfide phosphors will degrade under vacuum. The rare-earth sesquioxides, which exhibit sharp emission lines, high efficiency and stability in high vacuum, have received increasing attention and their luminescence properties have been investigated [3-5]. The europium(III)-doped Gd_2O_3 phosphor, $Gd_2O_3:Eu^{3+}$ ($Gd_{2-x}Eu_xO_3$) is an attractive red-emitting rare-earth sesquioxide phosphor with potential applications in various lighting and display devices [6, 7]. Both Gd_2O_3 and Eu_2O_3 have three different crystal structures: cubic, monoclinic and hexagonal. It is reported that the smaller electronegativity of Gd^{3+} facilitates charge transfer from the 2p orbital of O^{2-} to the 4f orbital of Eu^{3+}, and the $^8S \rightarrow {}^6D$ and $^8S_{7/2} \rightarrow {}^6I_J$ transitions of Gd^{3+} overlap in the charge transfer band (CTB), which leads to efficient energy transfer from Gd^{3+} to Eu^{3+} in $Gd_{2-x}Eu_xO_3$. Thus, cubic $Gd_{2-x}Eu_xO_3$ can exhibit a stronger and red-shifted CTB of the charge transfer edge, which allows sharper red emission at 611 nm than the monoclinic phase [8, 9]. However, for practical applications, further improvement in the red emission intensity is required for $Gd_{2-x}Eu_xO_3$. There are two main approaches to improve the luminescence properties of $Gd_{2-x}Eu_xO_3$: control of the morphology and/or structure, and doping with hetero-element ions. Several phosphors such as $Gd_{2-x}Eu_xO_3$ nanotubes [10], nanowires [11] and nanospherical particles [12] have been fabricated by the first approach. However, during the preparation of nanometer-sized $Gd_{2-x}Eu_xO_3$, many chemical reagents such as urea and dispersants are used, which introduces impurity ions and leads to the formation of non-radiative centers, and special equipment such

as autoclaves is required for synthesis under high pressure. For the doping approach, alkali metal ions are useful dopants to enhance the emission intensity because of the flux effect and the formation of oxygen vacancies [2, 13-15]. Moreover, the lithium cation (Li^+) is an attractive secondary dopant (compared with the Na^+ and K^+) for phosphors because its ionic radius is smaller than that of Gd^{3+}, which contributes to induce local distortion of the crystal field surrounding the Eu^{3+} activator.

$Gd_{2-x}Eu_xO_3$ is also expected to be applied as a high-temperature thermographic phosphor to detect temperatures, based on variation of the photoluminescence (PL) emission intensity with temperature, or the temperature dependence of the PL signal decay time [16, 17]. However, only the cubic phase of $Gd_{2-x}Eu_xO_3$ exhibits suitable PL properties. At ambient pressure, the transition temperature from the cubic to monoclinic phase of Gd_2O_3 is 1172-1250 ℃, and that from the monoclinic to hexagonal phase is approximately 2170 ℃ [8, 18]. On account of the phase transition temperature, most of the literature reports annealing temperatures lower than 1250 ℃, to maintain the cubic phase of $Gd_{2-x}Eu_xO_3$. Gao *et al*. [6] reported that $Gd_{2-x}O_3:Eu^{3+}_x$ left at room temperature under ambient pressure for two years transformed from the cubic phase to the monoclinic phase due to a gradual release of the residual stresses developed during synthesis. If there is a method to enhance the thermal stability of cubic phase $Gd_{2-x}Eu_xO_3$ to higher than 1250 ℃ at ambient pressure, then cubic $Gd_{2-x}Eu_xO_3$ could be utilized for thermal detection over a wider temperature range and degradation during long-term utilization could be avoided.

However, to our knowledge, no one has reported on the simultaneous enhancement of the luminescence and thermal stability of $Gd_{2-x}Eu_xO_3$. In the present work, cubic $Gd_{1.88}Eu_{0.12}O_3$ phosphors were synthesized by the solid state reaction method with doping different amounts of Li^+ (0 to 12 mol%). The PL properties and the thermal stability of cubic Li^+-doped $Gd_{1.88}Eu_{0.12}O_3$ were systematically investigated.

2.2. Experimental details

Li^+-doped cubic $Gd_{1.88}Eu_{0.12}O_3$ powders were synthesized by the solid solution method following the procedure reported by Dhananjaya *et al*. [14]. Gadolinium oxide (Gd_2O_3), europium oxide (Eu_2O_3) and lithium carbonate (Li_2CO_3) were used as starting materials. All the powders were purchased from Mitsuwa Chemical Company, Japan (99.99% purity). In a typical synthesis, appropriate amounts of Gd_2O_3 and Eu_2O_3 were mixed with Li_2CO_3 as a source of Li^+ from 0 to 12 mol% ($Li^+mol\% = \frac{Li^+mol}{Gd^{3+}mol + Eu^{3+}mol}$) and then stirred in 5 mL of ethanol for 10 min. The mixed powder was placed into a drying furnace at 100 ℃ for 5 min to remove the ethanol. The dried powder was heat-treated at temperatures in the range from 500 to 1300 ℃ in air for 3 h. To study the thermal stability of Li^+-doped cubic $Gd_{1.88}Eu_{0.12}O_3$, additional heat treatment at 1300 ℃ was performed on the samples synthesized at 1200 ℃.

Room temperature X-ray diffraction (XRD; X`pert Pro α1, Philips) analysis was performed on the heat-treated samples using Cu Kα radiation (λ=0.15405 nm).

The morphology of the heat-treated samples was observed using a scanning electron microscope (SEM; JSN-6360LV, Jeol) at 25 kV acceleration voltages. PL excitation and emission spectra were recorded using a spectrophotometer (F-7000, Hitachi) with a 150 W Xenon lamp as the excitation source. The PL internal and external quantum efficiencies for the light emission materials were measured through PL measurements using 60 mm integrated sphere. The Li^+ content in the phosphors was determined using inductively coupled plasma spectroscopy (ICP). The specific surface area (SSA) of the heat-treated samples was measured using a nitrogen (N_2) sorption apparatus (FlowSorb III 2310, Shimadzu Corporation) and evaluated by the Brunauer-Emmett-Teller (BET) method.

2.3. Results and discussion

2.3.1. Effect of Li^+-doping on morphology and PL properties of cubic $Gd_{1.88}Eu_{0.12}O_3$

Figure 2-1 (a) shows the PL excitation spectrum ($\lambda_{em.}$ = 611 nm) and emission spectrum ($\lambda_{ex.}$ = 254 nm) for cubic $Gd_{1.88}Eu_{0.12}O_3$ synthesized at 1200 ℃ for 3 h, while Figure 2-1 (b) shows those for monoclinic $Gd_{1.88}Eu_{0.12}O_3$. The excitation spectrum has three main peaks at 245, 255 and 277 nm. The highest peak at 245 nm is attributed to the charge transfer band (CTB) between O^{2-} and Eu^{3+} [8, 9]. The peaks at 255 nm and 277 nm superimposed on the CTB of Eu^{3+} are due to the Gd_2O_3 host excitation, and are assigned to the ^8S-^6D and ^8S-^6I transitions of Gd^{3+}, respectively. The weak peak at 311 nm can be assigned to the ^8S-^6P transition of Gd^{3+}. The peaks in the excitation spectrum indicate the energy transfer from Gd_2O_3 and Gd^{3+} to the doped Eu^{3+}. On the other hand, the several weak peaks over the range of 350-400 nm are due to the direct excitation of the Eu^{3+} ground state into the higher level of the 4*f* orbital [19].

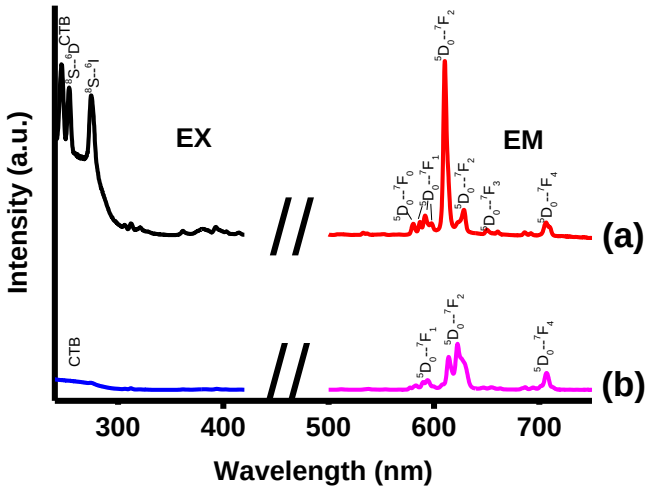

Fig. 2-1. Excitation and emission spectra for (a) cubic $Gd_{1.88}Eu_{0.12}O_3$ synthesized at 1200 ℃ for 3 h, and (b) monoclinic $Gd_{1.88}Eu_{0.12}O_3$ synthesized at 1300 ℃ for 3 h.

Under excitation of the CTB of Eu^{3+} at 245 nm, typical $^5D_0 \rightarrow {}^7F_J$ (J=0-4)

transitions of Eu^{3+} at 580, 591, 611 and 628 nm are observed in the PL emission spectrum. The weak emission peak at 580 nm can be assigned to the $^5D_0 \rightarrow ^7F_0$ transition and the peak at 591 nm is due to the $^5D_0 \rightarrow ^7F_1$ magnetic dipole transition. The most intensive emission peak at 611 nm and another weak peak at 628 nm are attributed to the $^5D_0 \rightarrow ^7F_2$ electric dipole transition. Thus, cubic $Gd_{1.88}Eu_{0.12}O_3$ exhibits red emission.

Li^+ doping was examined to enhance the PL red emission intensity of cubic $Gd_{1.88}Eu_{0.12}O_3$. The PL emission spectra for the 1200 ℃-synthesized phosphors doped with different amount of Li^+ were shown in Figure 2-2 (a), and the intensity of the dominant PL red emission peak at 611 nm for the samples was evaluated relative to the maximum luminescence intensity achieved for the 12 mol% Li^+ doped-sample, and is plotted in Figure 2-2 (b) as a function of the Li^+ content.

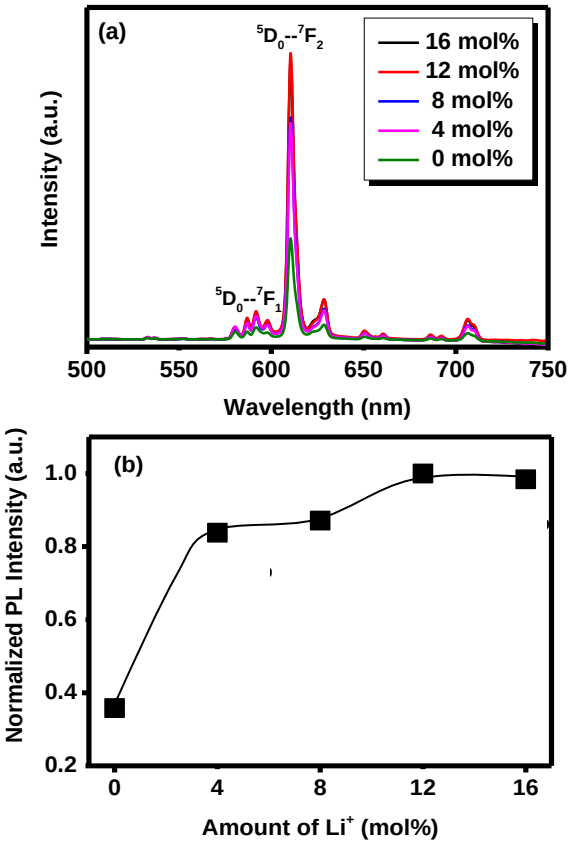

Fig. 2-2. PL emission properties of 1200 ℃-synthesized Li^+-doped $Gd_{1.88}Eu_{0.12}O_3$. (a) PL emission spectra for the $Gd_{1.88}Eu_{0.12}O_3$ doped with different amount of Li^+ and (b) the relative emission peak intensity at 611 nm for the $Gd_{1.88}Eu_{0.12}O_3$ as a function of the Li^+ content.

The dominant PL red emission peak intensity was significantly increased at 4 mol% Li^+, and then increased slightly from 8 to 12 mol% to reach a maximum at 12 to 16 mol%. This intensity was approximately 3 times higher than that for the undoped sample.

Table 2-1 summarizes the chemical composition analysis results for the 16 mol% Li^+-doped sample. For temperatures up to 600 ℃, the sample retained the starting Li^+ content. However, at 800 ℃ and above, the Li^+ content decreased consistently with increasing heat treatment temperature, due to the evaporation of Li^+ species from the sample. After heat treatment at 1200 ℃, no Li^+ species were detected in the sample. A series of four 1200 ℃-synthesized samples (0 (undoped), 4, 8 and 12 mol% Li^+-doped cubic $Gd_{1.88}Eu_{0.12}O_3$) were selected and their material properties were studied to clarify the intrinsic effects of Li^+-doping on the PL properties.

Table 2-1. Chemical composition of the heat-treated samples originally prepared with a nominal composition of 16 mol% Li^+-doped $Gd_{1.88}Eu_{0.12}O_3$ ($Li_{0.16}Gd_{1.88}Eu_{0.12}O_3$).

Heat treatment temperature (^oC)	Experimental composition
600	$Li_{0.16}Gd_{1.88}Eu_{0.12}O_3$
800	$Li_{0.12}Gd_{1.88}Eu_{0.12}O_3$
1000	$Li_{0.01}Gd_{1.88}Eu_{0.12}O_3$
1200	$Li_{0.00}Gd_{1.88}Eu_{0.12}O_3$

Figure 2-3 shows the undoped cubic $Gd_{1.88}Eu_{0.12}O_3$ was composed of fine particles, approximately 250 nm in size. The microstructure of the cubic $Gd_{1.88}Eu_{0.12}O_3$ became coarser as the amount of Li^+-doping was increased, and the particle size range of the 12 mol% Li^+-doped sample was approximately 800 nm to 1.3 μm. As a typical microstructural feature, neck growth at the particle boundaries was apparent in the Li^+-doped samples, which strongly suggests that liquid

phase-assisted partial sintering occurred to minimize the surface free energy of the cubic $Gd_{1.88}Eu_{0.12}O_3$ particles during heat treatment at up to 1200 ℃. The degree of microstructural coarsening was further evaluated by measuring the specific surface area (SSA) of the sample powders. Figure 2-4 shows the SSA of undoped cubic $Gd_{1.88}Eu_{0.12}O_3$ was 2.23 m^2/g, and the SSA decreased with increasing Li^+ doping. At 12 mol% Li^+ doping, the SSA was as low as 0.269 m^2/g.

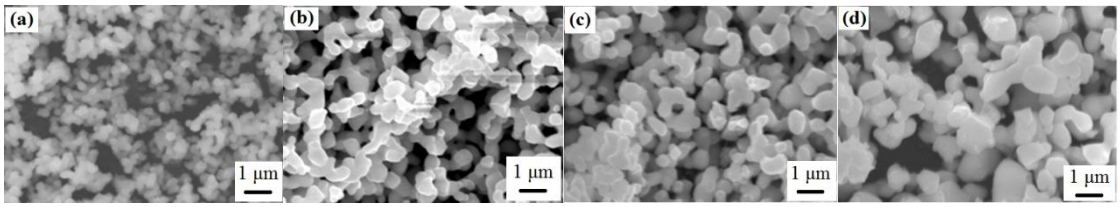

Fig. 2-3. SEM images of 1200 ℃-synthesized cubic $Gd_{1.88}Eu_{0.12}O_3$ doped with Li^+ at (a) 0, (b) 4, (c) 8, and (d) 12 mol%.

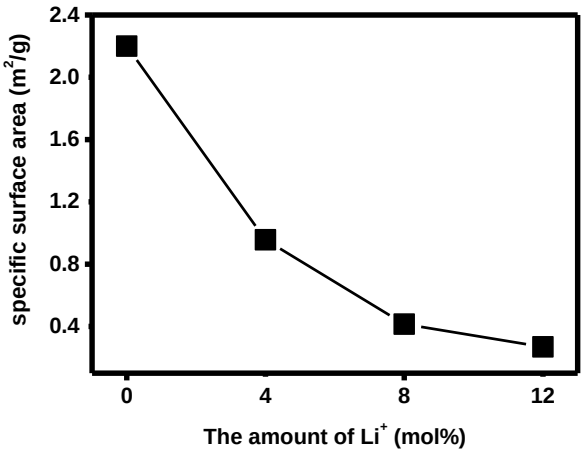

Fig. 2-4. SSA measured for 1200 ℃-synthesized cubic $Gd_{1.88}Eu_{0.12}O_3$ samples doped with various amounts of Li^+.

Figure 2-5 (a) shows XRD patterns for the 1200 ℃-synthesized samples. The diffraction peaks detected for each sample were identical to those for the standard powder diffraction file for cubic Gd_2O_3 (JCPDS No. 86-2477, space group: Ia-3). No additional crystalline phases containing Li^+ species were observed in the Li^+-doped samples, which is consistent with the ICP chemical composition analysis results shown in Table 2-1.

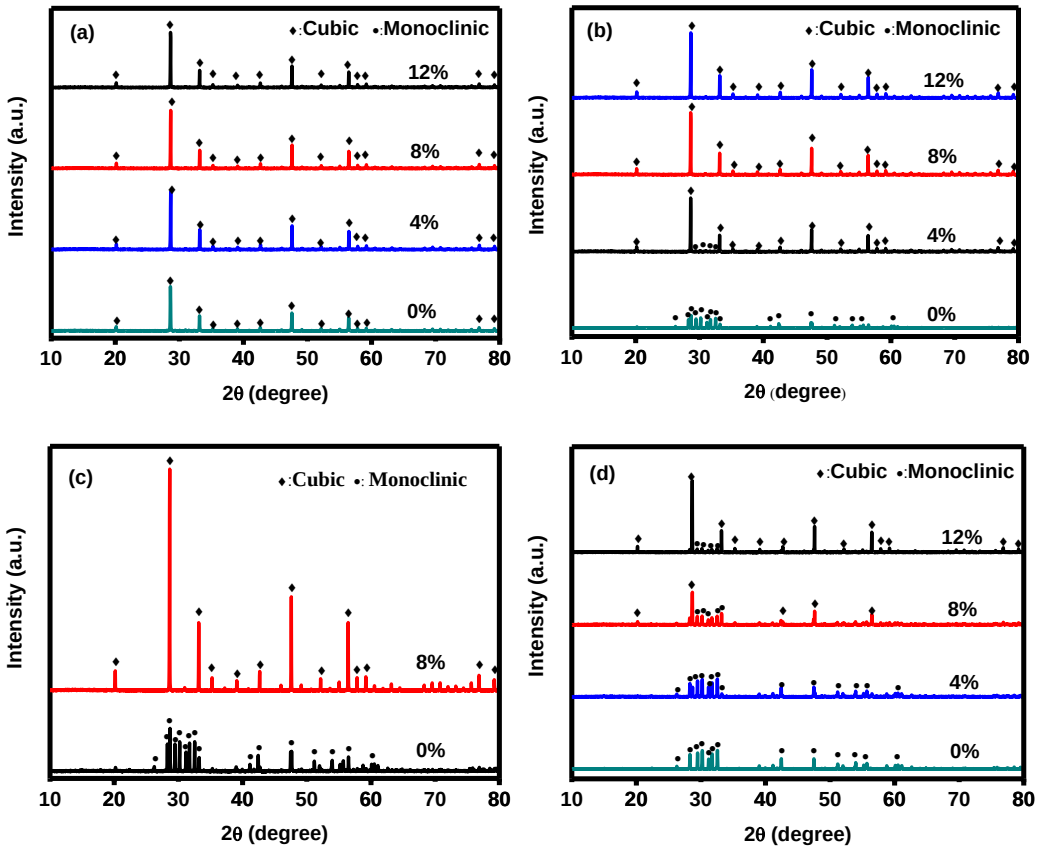

Fig. 2-5. XRD patterns for $Gd_{1.88}Eu_{0.12}O_3$ doped with various amounts of Li^+ and synthesized in air at (a) 1200 ℃ for 3 h, (b) 1300 ℃ for 3 h. (c) XRD patterns for (c) undoped and 8 mol% Li^+-doped Gd_2O_3 synthesized at 1300 ℃ for 3 h, and (d) $Gd_{1.88}Eu_{0.12}O_3$ doped with various amounts of Li^+, synthesized at 1200 ℃ for 3 h and subsequently annealed at 1300 ℃ for 72 h.

Besides the microstructural coarsening, the relative XRD peak intensity for the cubic $Gd_{1.88}Eu_{0.12}O_3$ was found to increase by the Li^+ doping as shown in Figure 2-6 (a). In this study, the XRD peak intensity was evaluated by measuring the sum of the intensities of the ten characteristic diffraction peaks of cubic $Gd_{1.88}Eu_{0.12}O_3$. The highest value was measured for $Gd_{1.88}Eu_{0.12}O_3$ doped with 12 mol% of Li^+ and a heat treatment at 1100 ℃. This value was set as 100%, and the sums of the peak intensities for the other samples were evaluated relative to this. The relative cubic phase intensity for the undoped sample heat-treated up to 800 ℃ was 40%. At 1200 ℃, the relative intensity was approximately 70%. At 1300 ℃, the cubic/monoclinic phase

transformation was completed, as shown in Fig. 2-5 (b), and no cubic phase was detected. The relative cubic phase intensities for the Li^+-doped samples were almost the same at all temperatures and were higher than that for the undoped sample above 500 ℃. At 1100 to 1200 ℃, the intensities reached 98-100%. As shown in Fig. 2-5 (b), even at 1300 ℃, the dominant phase of the Li^+-doped samples was cubic, and the relative cubic phase peak intensities were approximately 92%. The decrease in the intensity is considered to be due to the partial cubic to monoclinic phase transformation, which was detected for the 4 mol% Li^+-doped sample, as shown in Fig. 2-5 (b).

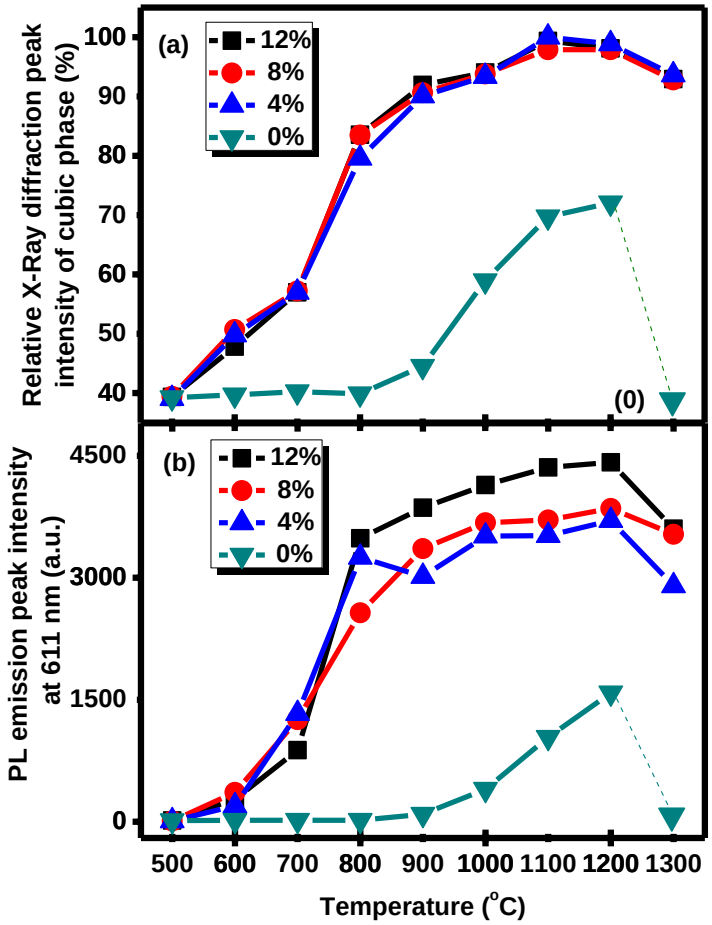

Fig. 2-6. Relationship between the heat treatment temperature in air and (a) relative XRD peak intensities of cubic phase, and (b) PL emission peak intensity at 611 nm evaluated for undoped and Li^+-doped $Gd_{1.88}Eu_{0.12}O_3$ (3 h heat-treatment).

The Li^+ source used in this study was Li_2CO_3 with a melting point of 618 ℃. Above this temperature, the resulting system, such as Li_2CO_3-Li_2O, could react with

Gd_2O_3 and Eu_2O_3 to form a eutectic liquid. Most of the Li^+ species evaporated from the samples up to 1000 ℃, as shown in Table 2-1; therefore, a certain amount of the eutectic liquid could be formed at 600 to 1000 ℃, which would lead to the enhanced growth of cubic $Gd_{1.88}Eu_{0.12}O_3$ polycrystallites caused by Ostwald ripening [20] as a result of the flux effect.

Figure 2-6 (b) shows the PL emission peak intensities at 611 nm for the four samples heat-treated at temperatures ranging from 500 to 1300 ℃. The intensity of the dominant PL red emission peak for the undoped sample was well correlated with the relative cubic phase intensity shown in Fig. 2-6 (a), and rapidly increased above 800 ℃ to reach a maximum at 1200 ℃. However, at 1300 ℃, the red emission peak intensity was negligible, which is attributed to the intrinsic extremely low PL emission efficiency of monoclinic $Gd_{1.88}Eu_{0.12}O_3$, as shown in Fig. 2-1 (b).

The red emission intensity for each Li^+-doped sample also increased with the relative cubic phase intensity, and reached a maximum at 1200 ℃, then decreased at 1300 ℃. Among the three Li^+-doped samples, the red emission peak intensity for the 12 mol% Li^+-doped sample was slightly higher than those for the two other samples heat-treated at 900 to 1200 ℃.

In this study, the PL red emission intensity was increased by the growth of cubic $Gd_{1.88}Eu_{0.12}O_3$ polycrystallites, which is similar to the results obtained in our previous study on $LiAl_5O_8:Eu^{3+}$ [21]. Evaluation of the internal quantum efficiency (IQE) and external quantum efficiency (EQE) was performed for the undoped and 12 mol% Li^+-doped samples. The IQE and EQE for the undoped sample were 69 and 29.2%, respectively, while those for the 12 mol% Li^+-doped sample were 85 and 60.9%, respectively. In particular, the EQE was significantly improved by the growth of cubic $Gd_{1.88}Eu_{0.12}O_3$ crystallites. As an idiographic factor to improve the EQE, larger $Gd_{1.88}Eu_{0.12}O_3$ crystallites could reduce the scattering effect and improve the photon absorption efficiency. The effect of Li^+ doping on the PL red emission intensity was further studied by evaluation of the asymmetry ratio. The emission for the $^5D_0$–$^7F_2$ transition at 611 nm is due to an electric dipole transition that is only allowed by the lack of inversion symmetry at the Eu^{3+} site [22], while that due to the $^5D_0$–$^7F_1$

transition at 591 nm is attributed to a magnetic dipole transition, which is not affected by the inverse site symmetry. It is well known that the relative intensities of the $^5D_0$-$^7F_1$ and $^5D_0$-$^7F_2$ emissions are strongly dependent on the local symmetry of Eu^{3+}, and the $^5D_0$-$^7F_2$/$^5D_0$-$^7F_1$ emission intensity ratio (asymmetry ratio) indicates the degree of distortion from the inversion symmetry of the local environment around the Eu^{3+} ion in the host lattice [23]. Figure 2-7 shows that the asymmetry ratio evaluated for the 1200 ℃ heat-treated samples increases monotonically with the amount of Li^+ doping.

In the cubic structure of Gd_2O_3, Gd^{3+}/Eu^{3+} ions are located in two crystallographically nonequivalent sites with 6-fold coordination [24]. The C_2 symmetry site has Gd^{3+}/Eu^{3+} in the center of a distorted cube with two oxygen vacancies on the face diagonal, while the S_6 symmetry site is the inversion symmetry that results from two oxygen vacancies lying on the body diagonal [20,25,26]. The dominant PL red emission peak at 611 nm attributed to the electric dipole transition is allowed only on the condition that the Eu^{3+} ion occupies a site without an inversion center, *i.e.*, the C_2 site in the host cubic Gd_2O_3. The numbers of the C_2 and S_6 sites in one unit cell of cubic Gd_2O_3 sites are typically 24 and 8, respectively, and the C_2/S_6 site ratio is determined as 3.

The ionic radii of Gd^{3+} and Eu^{3+} are 0.094 and 0.095 nm, respectively [27]. The difference between the two ionic radii is as low as 1.05%; therefore, Gd_2O_3 and Eu_2O_3 with the same group space (Ia-3) can form solid solutions at any proportion, and the occupation probabilities of the Eu^{3+} ion in the two symmetric sites are the same [28]. However, as shown in Fig. 2-7, the asymmetric ratio increases with the amount of the Li^+ doping. In addition to an enhancement of cubic $Gd_{1.88}Eu_{0.12}O_3$ crystallite growth, the C_2/S_6 site ratio occupied by Eu^{3+} ions increases with the amount of Li^+ doping in the range from 0 to 12 mol%.

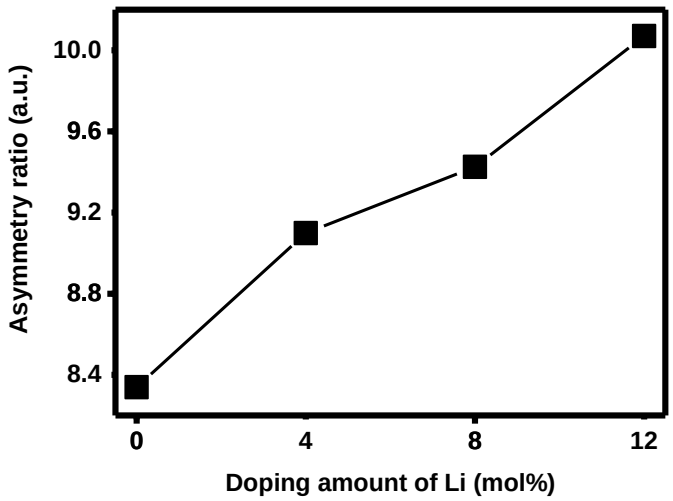

Fig. 2-7. Asymmetry ratio of the 1200 ℃-synthesized cubic $Gd_{1.88}Eu_{0.12}O_3$ as a function of the Li^+ content.

2.3.2. Enhanced thermal stability of cubic $Gd_{1.88}Eu_{0.12}O_3$ by Li^+ doping

The thermal stability of cubic $Gd_{1.88}Eu_{0.12}O_3$ was found to be significantly improved by Li^+ doping. After heat treatment at 1300 ℃ (higher than the reported cubic/monoclinic phase transition temperature of 1250 ℃), the dominant phase in the Li^+-doped samples was cubic (Fig. 2-5 (b)). To exclude the effect of Eu^{3+} ions on the thermal stability, Eu^{3+} ion-free 8 mol% Li^+-doped Gd_2O_3 and pure Gd_2O_3 were heat-treated at 1300 ℃ under the same conditions. Figure 2-5 (c) shows that 8 mol% Li^+-doped Gd_2O_3 exhibited typical diffraction lines identical to cubic Gd_2O_3, while the cubic/monoclinic phase transformation of pure Gd_2O_3 was completed. Therefore, these results indicate that the thermal stability of both cubic Gd_2O_3 and cubic $Gd_{1.88}Eu_{0.12}O_3$ can be improved by Li^+ doping.

To examine the potential for high-temperature applications, the 1200 ℃-synthesized cubic $Gd_{1.88}Eu_{0.12}O_3$ samples were annealed at 1300 ℃ for up to 72 h and the phase transformation behavior was monitored. As shown in Fig. 2-5 (d), the dominant phase for the 12 mol% Li^+-doped $Gd_{1.88}Eu_{0.12}O_3$ after 72 h was cubic, and compared with the 8 mol% and 4 mol% Li^+-doped samples, the thermal stability

of cubic $Gd_{1.88}Eu_{0.12}O_3$ was significantly improved. The cubic/monoclinic phase transformation behavior of the four samples during annealing at 1300 ℃ is shown in Fig. 2-8. Initially, all four samples were single phase cubic, as shown in Fig. 2-5 (a), and the phase transformation of these samples began within the first 3 hours. However, the phase transformation rate decreased with increasing Li^+ doping. The times to complete the phase transformation for the undoped and 4 mol% Li^+-doped samples were 3 and 36 h, respectively. In contrast, the relative cubic phase fractions of 40 and 90% remained in the 8 mol% and 12 mol% Li^+-doped samples, respectively, even after annealing for 72 h.

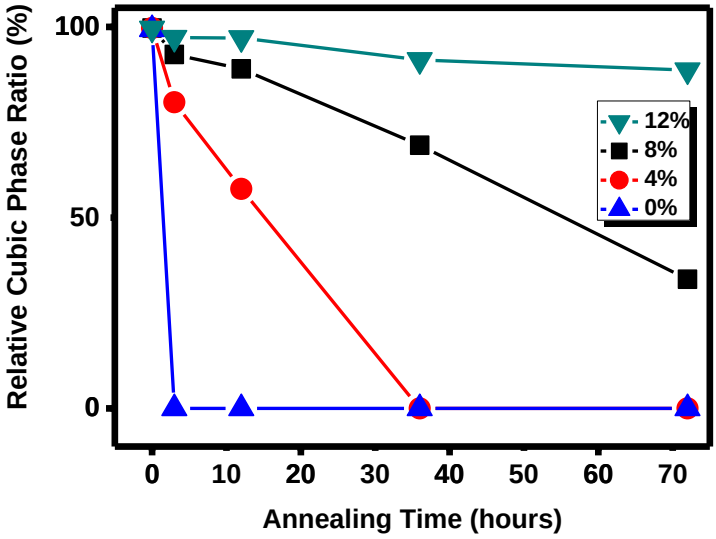

Fig. 2-8. Variety of the cubic phase ratio during additional heat-treatment at 1300 ℃ for the 1200 ℃-synthesized $Gd_{1.88}Eu_{0.12}O_3$ samples doped with various amounts of Li^+.

The enhanced thermal stability of the cubic phase is considered to be due to the presence of impurities and/or lattice defects, which increase the energy to complete the phase transformation, as previously discussed for quartz [29]. However, the 1200 ℃-synthesized cubic $Gd_{1.88}Eu_{0.12}O_3$ samples were free from Li^+; therefore, the role of Li^+ as an impurity can be excluded, while one possible reason to explain the enhanced thermal stability is the formation of additional oxygen vacancies. Li^+ is considered to be sufficiently small to diffuse into the host Gd_2O_3 lattice, which could promote the formation of oxygen vacancies to compensate for the valence difference

between Li^+ and Eu^{3+}. The number of additional oxygen vacancies is thus considered to increase with the amount of Li^+-doping, which leads to an increase in the degree of local distortion around the Eu^{3+} ion in the host Gd_2O_3 lattice, as evident from the increase in the asymmetric ratio. As a result, the C_2/S_6 site ratio occupied by Eu^{3+} ions increased with the amount of Li^+ doping.

2.4. Conclusions

In this study, cubic $Gd_{1.88}Eu_{0.12}O_3$ powders were synthesized by the solid state reaction method at 1200 ℃, and the effect of Li^+ doping on their PL properties and thermal stability was investigated. The results are summarized as follows:

(1) Under excitation of the CTB of Eu^{3+} at 245 nm, cubic $Gd_{1.88}Eu_{0.12}O_3$ exhibits a dominant PL emission peak at 611 nm, which is attributed to the electric dipole transition $^5D_0 \rightarrow {}^7F_2$ of Eu^{3+}.

(2) The dominant PL red emission peak intensity increased with the amount of the Li^+ doping and achieved a maximum for Li^+-doping from 12 to 16 mol%. This intensity was approximately 3 times higher than that for the undoped sample.

(3) The PL red emission peak intensity increased with the heat treatment temperature and reached a maximum at 1200 ℃. This behavior was well correlated with the temperature dependency of the relative intensity evaluated from the XRD peaks attributed to cubic $Gd_{1.88}Eu_{0.12}O_3$.

(4) ICP analysis results revealed that the doped Li^+ was completely evaporated from the sample during heat treatment up to 1200 ℃, while at 600 to 1000 ℃, Li^+-doping could promote the formation of a liquid phase, which enhanced the crystallite growth of cubic $Gd_{1.88}Eu_{0.12}O_3$ by Ostwald ripening. As a result, the relative XRD peak intensity of the cubic phase increased by the Li^+-doping in the range from 4 to 12 mol%.

(5) The IQE and EQE for 12 mol% Li^+-doped cubic $Gd_{1.88}Eu_{0.12}O_3$ were 85 and 60.9%, respectively. In particular, the EQE was significantly improved by the growth of cubic $Gd_{1.88}Eu_{0.12}O_3$ polycrystallites, which was achieved by a reduction of the scattering effect, thereby improving the photon absorption efficiency.

(6) As another effect of Li^+ doping on the PL properties, the asymmetric ratio evaluated for the PL emission spectrum of cubic $Gd_{1.88}Eu_{0.12}O_3$ monotonically increased with the amount of Li^+ doping in the range from 4 to 12 mol%.

(7) In addition to the enhanced PL emission intensity, the thermal stability of the cubic $Gd_{1.88}Eu_{0.12}O_3$ was significantly improved with increasing Li^+ doping, and even after annealing for 72 h at 1300 ℃, which exceeds the cubic/monoclinic phase transformation temperature, the relative fraction of the cubic phase in the 12 mol% Li^+ -doped sample was measured to be 90%.

(8) The improved thermal stability of the cubic phase at 1300 ℃ could be explained by the formation of additional oxygen vacancies, which increases the energy to complete the cubic/monoclinic phase transformation. The number of additional oxygen vacancies was considered to be increased with the amount of Li^+ doping. This could lead to an enhancement of the local environment distortion around the Eu^{3+} ion in the host Gd_2O_3, which was evaluated as the asymmetric ratio.

References

[1] B. K. Grandhe, V. R. Bandi, K. Jang, S. Kim, D. Shin, Y. Lee, J. Lim, T. Song, Met. Mater. Int. 3 (2013) 507.

[2] J. Park, H. Moon, D. Kim, S. Byeon, B. Kim, K. Suh, Appl. Phys. Lett. 77 (2000) 2162.

[3] C. Lin, K. Lin, Y. Li, J. Lumin. 126 (2007) 795.

[4] M. Hong, J. Kwo, A. Kortan, J. Mannaerts, A. Sergent, Science 283 (1999) 19.

[5] X. Wang, X. Sun, D. Yu, B. Zou, Y. Li, Adv. Mater. 15 (2003) 17.

[6] S. Gao, H. Lu, Y. Nie, H. Chen, D. Xu, Q. Dai, J. Zhang, C. Gao, S. Kan, D. Li, G. Zou, Mater. Lett. 61 (2007) 4003.

[7] H. Xiao, P. Li, F. Jia, L. Zhang, J. Phys. Chem. C 113 (2009) 21034.

[8] J. Li, Q. Zhu, X. Li, X. Sun, Y. Sakka, Acta Mater. 59 (2011) 3688.

[9] S. Choi, B. Park, T. Ahn, J. Kim, C. Hong, M. Yi, H. Jung, Thin Solid Films 519 (2011) 10.

[10] L. Liu, E. Ma, R. Li, G. Liu, X. Chen, Nanotechnology 18 (2007) 015403.

[11] K. Lin, Y. Li, Nanotechnology 17 (2006) 4048.

[12] A. Pires, M. Davolos, C. Santos, E. Stucchi, J. Flor, J. Solid State Chem. 171 (2003) 420.

[13] M. Ko, J. Park, D. Kim, S. Byeon, J. Lumin. 104 (2003) 215.

[14] N. Dhananjaya, H. Nagabhushana, B. Nagabhushana, B. Rudraswamy, C. Shivakumara, R. Chakradhar, J. Alloys Compd. 509 (2011) 2368.

[15] N. Dhananjaya, H. Nagabhushana, B. Nagabhushana, B. Rudraswamy, C. Shivakumara, K. Narahari, R. Chakradhar, Spectrochim. Acta A 86 (2012) 8.

[16] R. Ranson, E. Evangelou, C. Thomas, Appl. Phys. Lett. 72 (1998) 2663.

[17] C. Brites, P. Lima, N. Silva, A. Millan, V. Amaral, F. Palacio, L. Carlos, Adv. Mater. 22 (2010) 4499.

[18] M. Zinkevich, Prog. Mater. Sci. 52 (2007) 597.

[19] A. Zhang, M. Lü, G. Zhou, Y. Zhou, Z. Qiu, Q. Ma, J. Alloys Compd. 468 (2009) 17.

[20] W. Ostwald, Z. Phys. Chem. 37 (1901) 385.

[21] M. Aoyama, Y. Amano, K. Inoue, S. Honda, S. Hashimoto, Y. Iwamoto, J. Lumin. 135 (2013) 211.

[22] T. Kano, "Luminescence centers of rare-earth ions," Phosphor Handbook, pp. 192 (1998).

[23] M. Nogami, T. Enomoto, T. Hayakawa, J. Lumin. 97 (2002) 147.

[24] E. Goldys, K. Tomsia, S. Jinjun, D. Dosev, I. Kennedy, S. Yatsunenko, M. Godlewski, J. Am. Chem. Soc. 128 (2006) 14498.

[25] M. Buijs, A. Meyerink, G.Blasse, J. Lumin. 37 (1987) 9.

[26] H. Forest, G. Ban, J. Electrochem. Soc. 116 (1969) 474.

[27] R. Shannon, Acta Cryst. 32 (1976) 751.

[28] C. Liu, S. Lu, B. Chen, J. Zhang, J. Liu, J. Lumin. 122 (2007) 80.

[29] Private communication: N. Koga, H. Muraishi, Annual Report of Faculty of Engineering, Kyushu Sangyo University, 42 (2006) 163.

CHAPTER 3: Photoluminescence and cathodoluminescence properties of Li^+ doped $Gd_{1.88}Eu_{0.12}O_3$

3.1. Introduction

Field Emission Displays (FEDs) have been widely used for televisions, personal computers and cell phones in our daily life to replace the conventional cathode ray tube (CRT) displays [1]. In the past decades, most of the interest has been focused on the materials for FEDs operating at low electron beam excitation voltages (≤10 kV) [2]. However, under the low excitation voltages, there is no ideal material with sufficient brightness, fast response and long term stability used for the modern luminescence devices [3]. Former researches have mainly used sulfide red phosphors such as $Y_2O_2S:Eu^{3+}$, $SrGa_2S_4:Eu^{3+}$, ZnS:Ag,Cl, (Zn/Cd)S:Cu etc. [4-7]. Unfortunately, the sulfide phosphors are unstable under electron bombarding in vacuum, which leads to the chemical degradation of phosphor layers and emit sulfide-containing gases under the operation condition [3, 8]. On the other hand, due to the sharp lines, high efficiency and stability in high vacuum, rare-earth sesquioxides have received increased attention and their luminescence properties have been investigated [9-11]. Europium(III)-doped Gd_2O_3 phosphor ($Gd_{2-x}Eu_xO_3$) is one of the attractive red emitting rare-earth sesquioxide phosphors with potential applications in various lighting and display devices [12]. Both Gd_2O_3 and Eu_2O_3 have three different kinds of cubic, monoclinic and hexagonal phases. It is reported that the smaller electronegativity of Gd^{3+} permits an easier charge transfer from the *2p* orbital of O^{2-} to the *4f* orbital of Eu^{3+}, and the $^8S \rightarrow {}^6D$ and $^8S_{7/2} \rightarrow {}^6I_J$ transitions of Gd^{3+} overlap in the charge transfer band (CTB), which leads to efficient energy transfer from Gd^{3+} to Eu^{3+} in $Gd_{2-x}Eu_xO_3$. Therefore, cubic $Gd_{2-x}Eu_xO_3$ exhibits stronger and red-shift CTB of the charge transfer edge, which allows sharper red emission at 611 nm than the monoclinic $Gd_{2-x}Eu_xO_3$ [13-14].

However, compared with commercial red phosphors like $Zn_{0.2}Cd_{0.8}S:Ag^+$ and $Y_2O_2S:Eu^{3+}$ [2], the red emission intensity of $Gd_{2-x}Eu_xO_3$ is not sufficient for practical applications. There are two main approaches to improve the luminescence properties

of $Gd_{2-x}Eu_xO_3$: morphology and/or structure controlling, and with hetero-element ions. Several $Gd_{2-x}Eu_xO_3$ phosphors like nanotubes [15], nanowires [16], and nanospherical particles [17] have been synthesized. However, during synthesis of the nanometer-sized $Gd_{2-x}Eu_xO_3$, lots of chemical reagents like urea and dispersant are used, which introduces impurity ions and leads to form non-radiation centers. For the second approach, alkali metal ions are useful dopants to enhance the emission intensity because of the flux effect and the formation of oxygen vacancies [2, 18-22]. Moreover, due to the radius smaller than the Gd^{3+}, Li^+ is an attractive secondary dopant (compare with the Na^+ and K^+) for host Gd_2O_3, which contributes to increase local distortion of the crystal field surrounding the Eu^{3+} activator [23]. As mentioned in Chapter 2, in our previous study on $Gd_{2-x}Eu_xO_3$ with optimized Eu^{3+} concentration of 12 mol% ($Gd_{1.88}Eu_{0.12}O_3$), the PL red emission intensity was found to increase approximately three times by Li^+-doping at 12 to 16 mol%. Moreover, the thermal stability of the cubic $Gd_{1.88}Eu_{0.12}O_3$ was significantly improved by the Li^+-doping, and even after annealing for 72 h at 1300 ℃, which exceeds the cubic/monoclinic phase transformation temperature, the relative fraction of the cubic phase in the 12 mol% Li^+ -doped $Gd_{1.88}Eu_{0.12}O_3$ was measured to be 90% [23].

As a part of our study on luminescent properties, PL and cathodoluminescence (CL) properties of Li^+-doped cubic $Gd_{1.88}Eu_{0.12}O_3$ were further studied. In the present work, Gd_2O_3-Eu_2O_3 mixed powder was prepared by using co-precipitation technique and cubic $Gd_{1.88}Eu_{0.12}O_3$ phosphors with different amounts of Li^+ were synthesized by heat treatment at 1200 ℃ in air for 3h. PL properties were evaluated by using a conventional spectrophotometer, while CL emission properties under low excitation voltage were investigated by mounting the synthesized $Gd_{1.88}Eu_{0.12}O_3$ phosphor on a vacuum fluorescent display (VFD). The resulting PL and CL properties were discussed by comparison with those synthesized by the conventional solid solution method.

3.2. Experimental procedures

3.2.1. Synthesis of Li^+-doped cubic $Gd_{1.88}Eu_{0.12}O_3$ phosphors

Gadolinium oxide (Gd_2O_3), europium oxide (Eu_2O_3) and lithium carbonate (Li_2CO_3) were used as starting powders. All the powders were purchased from Mitsuwa Chemical Company, Japan (99.99% purity). Appropriate amounts of Gd_2O_3 and Eu_2O_3 were completely dissolved in a HNO_3 aqueous solution with *pH* =1. Through the whole process, the aqueous solution was stirred by a magnetic stirrer. The precipitation was carried out by adding aqueous NH_4OH solution until the solution reached a *pH* of 8. The precipitate was separated by filtration and dried at 100 ^oC for 3 h. The dried powder was calcined at 1200 ^oC in air for 3 h. In a typical synthesis, a proper amount of the calcined powder was mixed with Li_2CO_3 as a source of Li^+ from 0 to 20 mol% ($Li^+mol\% = \frac{Li^+mol}{Gd^{3+}mol + Eu^{3+}mol}$). Then, the mixed powder (about 2 g) was stirred with 5 ml ethanol for 10 minutes and subsequently placed into a drying furnace at 100 ^oC for 5 min to remove the ethanol. The dried powder was heat-treated at 1200 ^oC in air for 3 h.

To study the effect of synthesis method on luminescence properties, Li^+-doped cubic $Gd_{1.88}Eu_{0.12}O_3$ phosphors were also synthesized by conventional solid solution method [19, 23]. Appropriate amounts of Gd_2O_3 and Eu_2O_3 were mixed with Li_2CO_3 and ethanol followed by stirring in the same manner shown above. After drying in a furnace at 100 ^oC, the mixed powder was heat-treated at 1200 ^oC in air for 3 h.

3.2.2. Characterizations

Room temperature X-ray diffraction (XRD; X`pert Pro α1, Philips) analysis was performed on the 1200 ^oC heat-treated samples using Cu Kα radiation (λ =0.15405 nm). The average crystallite size of $Gd_{1.88}Eu_{0.12}O_3$ phosphors was evaluated by the Scherrer equation [24-25]:

$$D = \frac{0.9\lambda}{B\cos\theta} \qquad (1)$$

where D is the average crystallite size, λ is the X-ray wavelength (λ=0.15405 nm), B is the full width at half maximum of the observed peak, and the factor of 0.9 for spherical objects was used in this study.

Morphology and microstructure of Li^+-doped $Gd_{1.88}Eu_{0.12}O_3$ phosphors was observed using a scanning electron microscope (SEM, JSN-6360LV, JEOL) at 25 kV acceleration voltages.

PL excitation and emission spectra were record by a spectrophotometer (F-7000, Hitachi) with a 150 W Xenon lamp as the excitation source. CL emission properties of the synthesized Li^+-doped $Gd_{1.88}Eu_{0.12}O_3$ phosphors were studied by mounting the phosphor on a VFD operated at an anode voltage of 50 VDC (Pulse Width of 100 msec. and Pulse Duty of 1/60 generated by FC110, YOKOGAWA, Japan) with an average current density of 1.3 mA/cm^2. The CL emission spectrum and the luminance intensity at room temperature were recorded and measured, respectively by a spectroradiometer (TOPCON SR-3A, Topcon Technohouse Corporation, Japan). This VFD mount test was performed at Noritake Itron Corporation, Japan.

3.3. Results and discussion

3.3.1. Crystalline phase and morphology

Powder XRD patterns for 1200 ^{o}C-synthesized $Gd_{1.88}Eu_{0.12}O_3$ synthesized by co-precipitation (CP) and solid solution (SS) methods are shown in Fig. 3-1. The diffraction peaks detected for each sample were identical to those for the standard powder diffraction file for cubic Gd_2O_3 (JCPDS No. 86-2477, space group: *Ia*-3). Even for the samples with 20 mol% Li^+, no additional crystalline phases containing Li^+ species were detected.

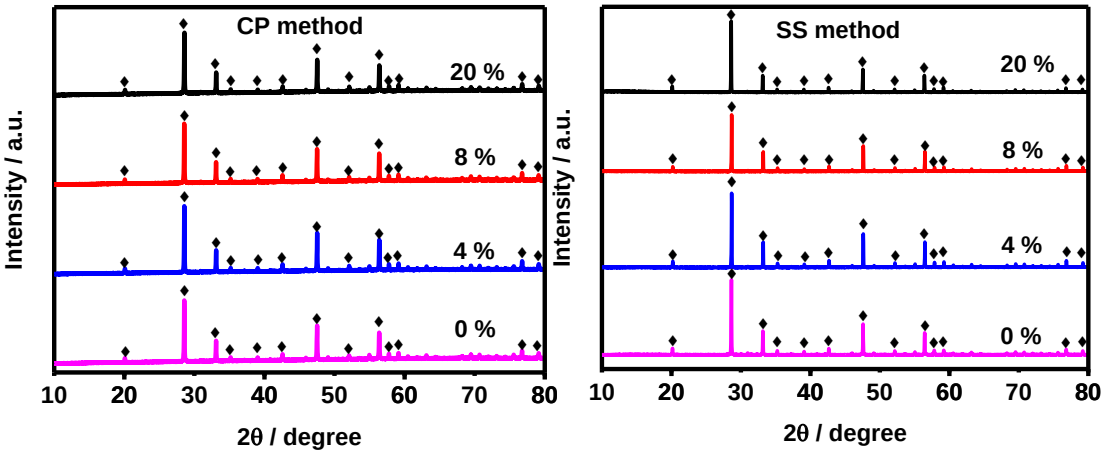

Fig. 3-1. XRD patterns for $Gd_{1.88}Eu_{0.12}O_3$ doped with different amounts of Li^+ synthesized by CP and SS methods after heat treatment at 1200 °C in air for 3h (♦ indicates cubic Gd_2O_3).

Figure 3-2 shows the average crystallite size for $Gd_{1.88}Eu_{0.12}O_3$ doped with different amounts of Li^+ synthesized by SS and CP methods, and typical SEM images of the $Gd_{1.88}Eu_{0.12}O_3$ are shown in Fig. 3-3. At all the amount of Li^+-doping from 0 to 20 mol%, the average crystallite size for the $Gd_{1.88}Eu_{0.12}O_3$ synthesized by CP method was close to that synthesized by SS method. The average crystallite size monotonously increased with increasing the amount of Li^+-doping. Finally at 20 mol%, the average crystallite size reached approximately 2.3 μm.

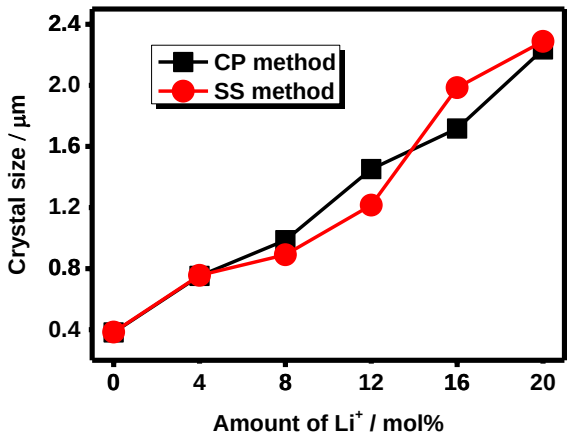

Fig. 3-2. Average crystallite size for $Gd_{1.88}Eu_{0.12}O_3$ doped with different amounts of Li^+ synthesized by CP and SS methods after heat treatment at 1200 °C in air for 3h.

The morphologies of the Li^+-doped $Gd_{1.88}Eu_{0.12}O_3$ synthesized by CP method

were similar to those synthesized by SS method. The Li^+-free sample was composed of round-shaped grains with several hundred nanometers in size. With increasing amount of Li^+-doping, the grain size increased and the neck growth at the grain boundaries became apparent. This microstructure coarsening could be due to the flux effect which promoted liquid phase-assisted sintering for minimizing the surface free energy of cubic $Gd_{1.88}Eu_{0.12}O_3$ grains (Fig. 3-3).

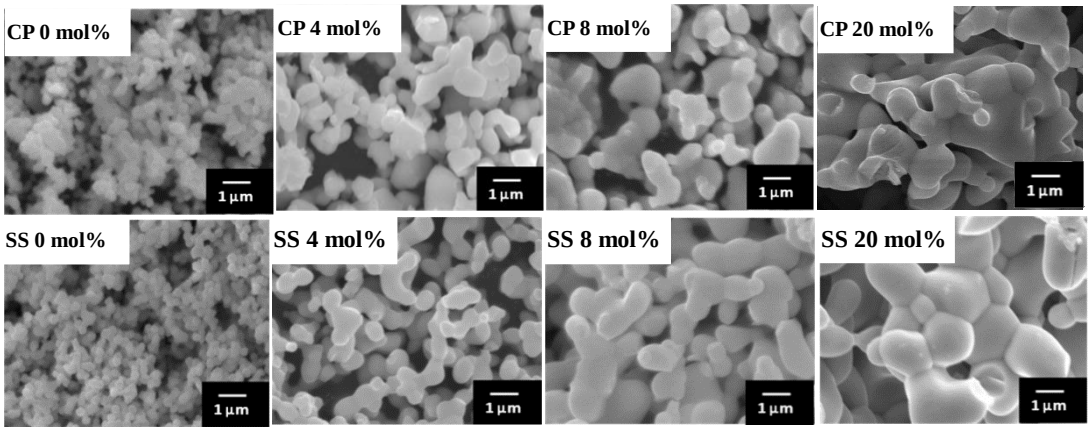

Fig. 3-3. SEM images of $Gd_{1.88}Eu_{0.12}O_3$ doped with different amounts of Li^+ synthesized by heat treatment at 1200 °C in air for 3h (CP and SS indicate CP method and SS method, respectively).

The degree of microstructural coarsening was further evaluated by measuring the specific surface area (SSA) of the $Gd_{1.88}Eu_{0.12}O_3$. The SSA values were plotted as a function of amount of Li^+-doping and are shown in Fig. 3-4. The SSA for the Li^+-free $Gd_{1.88}Eu_{0.12}O_3$ synthesized by SS method was 2.230 m^2/g, then decreased with increasing amount of Li^+ doping. At the 20 mol% Li^+-doping, SSA became as low as 0.254 m^2/g. The samples synthesized by CP method also showed the same tendency. However, at the Li^+ doping from 0 to 8 mol%, the SSA for $Gd_{1.88}Eu_{0.12}O_3$ synthesized by CP method was apparently lower than that by SS method. Above 8 mol%, SSA values were lower than 0.4 m^2/g and compatible with those synthesized by SS method.

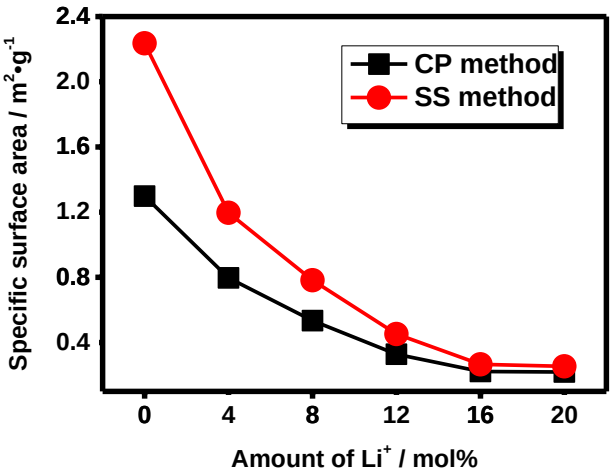

Fig. 3-4. Variation of specific surface area (SSA) for $Gd_{1.88}Eu_{0.12}O_3$ doped with different amounts of Li^+ synthesized by CP and SS methods.

3.3.2. PL properties

Figure 3-5 demonstrates PL excitation spectrum ($\lambda_{em.}$ = 611 nm) and emission spectrum ($\lambda_{ex.}$ = 245 nm) for 12 mol% Li^+-doped $Gd_{1.88}Eu_{0.12}O_3$ synthesized by CP method. The spectra were well consistent with those synthesized by SS method in our previous study [23] and the excitation spectrum exhibits three main peaks at 245, 255 and 277 nm. The highest peak at 245 nm is attributed to the charge transfer band (CTB) between O^{2-} and Eu^{3+} [13-14]. The peaks at 255 nm and 277 nm superimposed on the CTB of Eu^{3+} are due to the Gd_2O_3 host excitation, and are assigned to the $^8S \rightarrow {}^6D$ and $^8S \rightarrow {}^6I$ transitions of Gd^{3+}, respectively. The weak peak at 311 nm can be assigned to the $^8S \rightarrow {}^6P$ transition of Gd^{3+}. The peaks in the excitation spectrum indicate the energy transfer from Gd_2O_3 and Gd^{3+} to the doped Eu^{3+}. On the other hand, the several weak peaks at 350-400 nm are due to the direct excitation of the Eu^{3+} ground state into the higher level of the *4f* orbital [19].

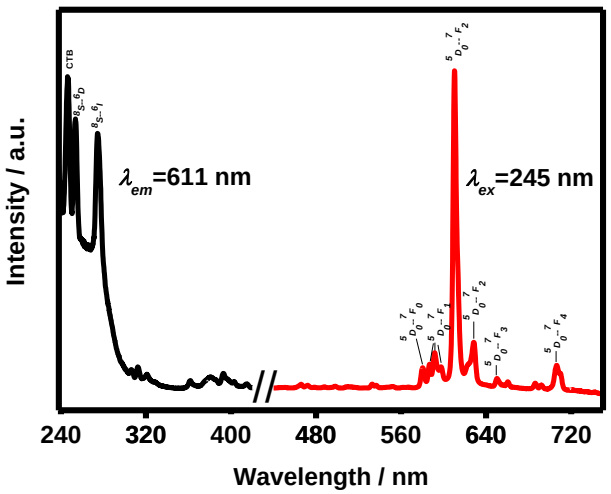

Fig. 3-5. PL excitation and emission spectra for 12 mol% Li^+-doped $Gd_{1.88}Eu_{0.12}O_3$ synthesized by CP method.

Upon an excitation at 245 nm, typical $^5D_0 \rightarrow {}^7F_J$ (J=0-4) transitions of Eu^{3+} at 580, 591, 611 and 628 nm are observed in the PL emission spectrum. The weak emission peak at 580 nm can be assigned to the $^5D_0 \rightarrow {}^7F_0$ transition and the emission peak at 591 nm is attributed to the $^5D_0 \rightarrow {}^7F_1$ magnetic dipole transition. The most intense emission peak at 611 nm and another weak peak at 628 nm are due to the $^5D_0 \rightarrow {}^7F_2$ electric dipole transition.

Typical PL emission spectra (λ_{ex} =245 nm) for the $Gd_{1.88}Eu_{0.12}O_3$ phosphors synthesized in this study are shown in Fig. 3-6. There was a tendency for the dominant red emission peak intensity at 611 nm to increase consistently with the amount of Li^+-doping. Then, the values of the peak intensity at 611 nm for the $Gd_{1.88}Eu_{0.12}O_3$ phosphors were plotted and analyzed. As shown in Fig. 3-7 (a), the intensity for the phosphor synthesized by SS method increased with increasing amount of Li^+-doping and reached a maximum at 20 mol% Li^+-doping. On the other hand, the intensity for the Li^+-free $Gd_{1.88}Eu_{0.12}O_3$ synthesized by CP method was high and compatible with that achieved for the 16 mol% Li^+-doped $Gd_{1.88}Eu_{0.12}O_3$ synthesized by SS method. Then, the intensity increased slightly to reach a maximum at 8 to 20 mol%, and was close to that for the 20 mol% Li^+-doped $Gd_{1.88}Eu_{0.12}O_3$ synthesized by SS method.

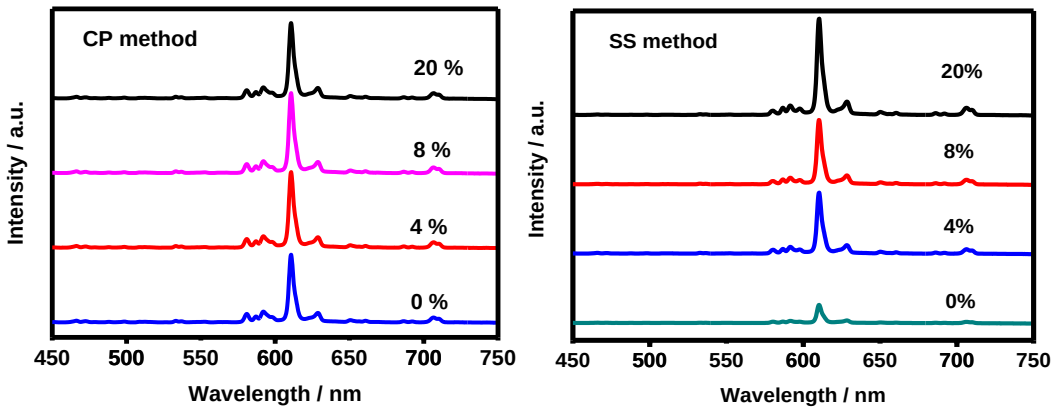

Fig. 3-6. PL emission spectra ($\lambda_{ex.}$ = 245 nm) for $Gd_{1.88}Eu_{0.12}O_3$ phosphors doped with different amounts of Li^+ synthesized by CP and SS methods.

The dominant emission peak at 611 nm due to the $^5D_0 \rightarrow {}^7F_2$ electric dipole transition is hypersensitive to the symmetry of local environment around Eu^{3+} ion [26], while that due to the $^5D_0 \rightarrow {}^7F_1$ transition at 591 nm is attributed to a magnetic dipole transition, which is not affected by the inverse site symmetry. It is well known that the relative intensities of the $^5D_0 \rightarrow {}^7F_1$ and $^5D_0 \rightarrow {}^7F_2$ emissions strongly depend on the local symmetry of Eu^{3+}, and the $^5D_0 \rightarrow {}^7F_2/{}^5D_0 \rightarrow {}^7F_1$ emission intensity ratio (asymmetry ratio) indicates the degree of distortion from the inversion symmetry of the local environment around Eu^{3+} ion in the host lattice [27]. In our previous study on Li^+-doped $Gd_{1.88}Eu_{0.12}O_3$ synthesized by SS method [23], it was experimentally demonstrated that the dominant PL red emission peak intensity at 611 nm was proportional to the asymmetric ratio, and the asymmetric ratio increased consistently with the amount of Li^+-doping. Then, the asymmetric ratios were evaluated for the phosphors synthesized by CP method. The values were plotted as a function of amount of Li^+-doping and compared with those synthesized by SS method. As shown in Fig. 3-7 (b), the asymmetric ratio increased with the amount of Li^+-doping, however at all the amount of Li^+-doping in the range of 0 to 20 mol%, the asymmetric ratio for $Gd_{1.88}Eu_{0.12}O_3$ synthesized by CP method was found to be lower than that synthesized by SS method.

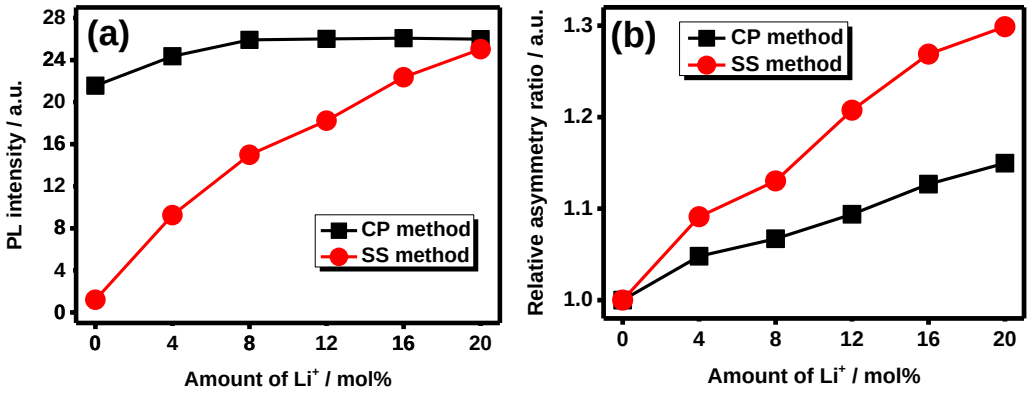

Fig. 3-7. PL emission properties of $Gd_{1.88}Eu_{0.12}O_3$ as a function of amount of Li^+-doping: (a) Dominant red emission intensity at 611 nm under UV excitation at 245 nm and (b) asymmetry ratio.

Generally, large surface area carries large number of defects into the host lattice. Defects have a serious drawback in PL emission intensity since they provide non-radiative recombination routes for the electrons and holes. If the defect density is sufficiently reduced by crystallite growth, PL emission intensity would be improved [20, 28-30]. In the present study, PL red emission intensity for the $Gd_{1.88}Eu_{0.12}O_3$ synthesized by SS method was successfully enhanced by host Gd_2O_3 crystallite growth via liquid phase-assist sintering. However, as shown in Figs. 3-2 and 3-3, the Li^+-free $Gd_{1.88}Eu_{0.12}O_3$ synthesized by CP method exhibited a fine-grained microstructure with an average crystallite size of approximately 400 nm. One possible reason for the high PL emission intensity is due to the improved dispersion property of Eu^{3+} ions doped in the host Gd_2O_3. During the synthesis process using co-precipitation technique, Gd_2O_3 and Eu_2O_3 were converted to $Gd(NO_3)_3$ and $Eu(NO_3)_3$, respectively. The resulting soluble salts could be well and uniformly mixed at the molecular level, which leading to minimize the energy trapped by the non-radiative recombination center during the energy migration process between one Eu^{3+} ion to another one caused by segregation of Eu^{3+} ions in the host Gd_2O_3. As a result, relatively high PL emission intensity was thought to be achieved for the $Gd_{1.88}Eu_{0.12}O_3$ at the Li^+-doping from 0 to 8 mol%.

3.3.3. CL properties

The Li^+-doped $Gd_{1.88}Eu_{0.12}O_3$ was mounted on a VFD, and under the VFD operating condition at an anode voltage of 50 V, CL properties were studied. As a typical result, figure 3-8 presents a CL emission spectrum for 8 mol% Li^+-doped $Gd_{1.88}Eu_{0.12}O_3$ synthesized by SS method. Characteristic emission peaks due to the *f-f* transition of Eu^{3+} ions are observed. The dominant emission peak is located at 611 nm assigned to the $^5D_0 \rightarrow {}^7F_2$ electric dipole transition of Eu^{3+}. Thus, the $Gd_{1.88}Eu_{0.12}O_3$ exhibits intense CL red emission under the VFD operating condition in this study.

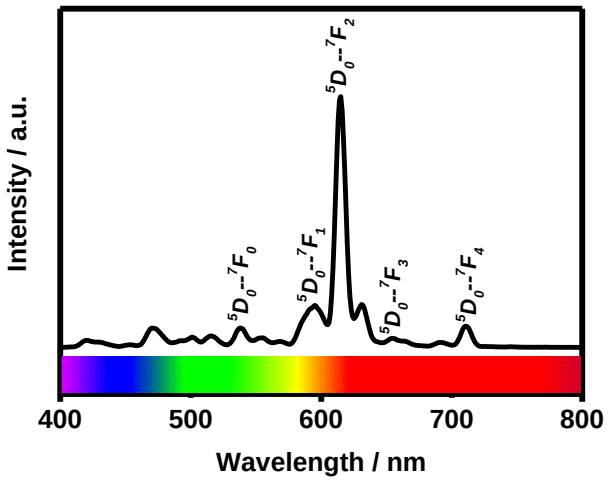

Fig. 3-8. CL emission spectrum under VFD operating condition at an acceleration voltage of 50 V for 8 mol% Li^+-doped $Gd_{1.88}Eu_{0.12}O_3$ synthesized by SS method.

Figure 3-9 (a) shows luminance intensity evaluated for the dominant CL red emission of Li^+-doped $Gd_{1.88}Eu_{0.12}O_3$. In contrast to the liner relation between the amount of Li^+ and PL emission intensity shown in Fig. 3-7 (a), Li^+-doped $Gd_{1.88}Eu_{0.12}O_3$ synthesized by SS method exhibited a maximum luminance intensity at 8 mol% Li^+, while above this amount, the intensity decreased with the amount of Li^+. On the other hand, when $Gd_{1.88}Eu_{0.12}O_3$ was synthesized by CP method, the initial luminance intensity (at 0 mol% Li^+) remarkably improved to 31.3 cd/m^2, and the intensity achieved a maximum at 4 mol% Li^+. However, this intensity (37.3 cd/m^2) was apparently lower than that achieved for the 8 mol% Li^+-doped $Gd_{1.88}Eu_{0.12}O_3$

synthesized by SS method (53.9 cd/m^2).

Figure 3-9 (b) demonstrates relation between the SSA and the luminance intensity for $Gd_{1.88}Eu_{0.12}O_3$ phosphors investigated in this study. Regardless of synthesis method, the luminance intensity reaches a maximum at around 0.8 m^2/g, while below this value, the intensity decreases with increasing amount of Li^+-doping.

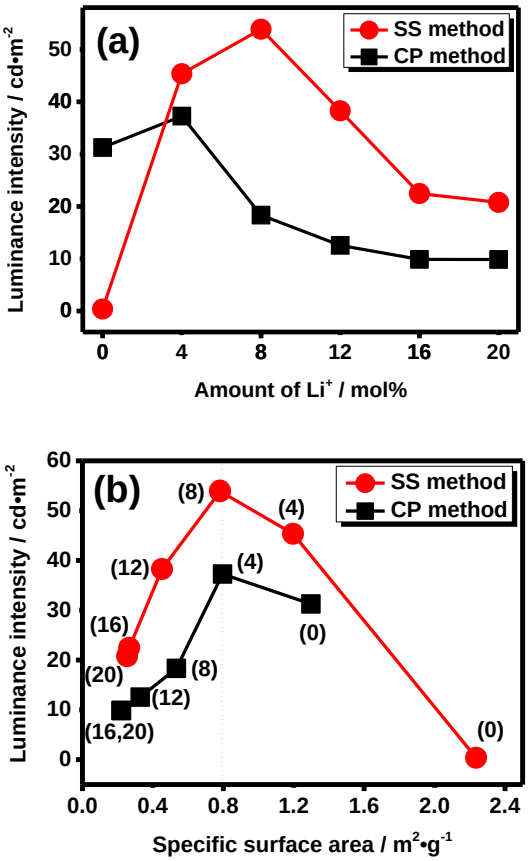

Fig. 3-9. CL emission properties of $Gd_{1.88}Eu_{0.12}O_3$ doped with different amounts of Li^+ synthesized by CP and SS methods: (a) Luminance intensity evaluated for the dominant CL red emission at 611 nm as a function of amount of Li^+-doping, and (b) Relation between SSA and luminance intensity for $Gd_{1.88}Eu_{0.12}O_3$ phosphors investigated in this study (Numbers in parentheses indicate the amount of Li^+ doping).

At electron beam excitation voltages ranging from 1 to10 kV, the penetration depth of electrons into the solid is well described by Feldman [31] using the high-energy excitation model. Based on the model, for example, Liu *et al*. reported that the electron penetration depth at 5 kV for rare-earth cation-doped $SrIn_2O_4$ was estimated as 67.44 nm [32]. At high excitation voltages, CL properties should be

governed by material factors such as crystallinity of host material and dispersion property of activator ions in the host lattice. On the other hand, under our present VFD operating condition at an anode voltage of 50 V, the electron penetration depth must be extremely shallow. Therefore, it is essentially required for enhancing the luminance intensity to maintain a sufficient surface area of a phosphor mounted in a VFD. In this study, crystallinity of $Gd_{1.88}Eu_{0.12}O_3$ and dispersion property of Eu^{3+} in the host lattice could be improved in association with decreasing surface area of $Gd_{1.88}Eu_{0.12}O_3$. Thus, the SSA value of 0.8 m^2/g is considered as an approximate lower limit that can offer possibilities for enhancing luminance intensity.

3.4. Summary

In this study, Li^+-doped $Gd_{1.88}Eu_{0.12}O_3$ phosphors were synthesized at 1200 ^oC in air by co-precipitation (CP) and solid solution (SS) methods. The PL and CL properties of the synthesized phosphors were studied and discussed based on the material factors in terms of the average crystallite size, dispersion property of Eu^{3+} ions in the host Gd_2O_3 and specific surface area (SSA). The results are summarized as follows:

(1) The average crystallite size for $Gd_{1.88}Eu_{0.12}O_3$ synthesized by CP method was closed to that synthesized by SS method at all the amount of Li^+-doping from 0 to 20 mol%. The average crystallite size at 0 mol% Li^+ was approximately 400 nm, then increased consistently with amount of Li^+-doping. The maximum average crystallite size achieved at 20 mol% Li^+ was about 2.3 μm.

(2) Under the excitation of charge transfer band between O^{2-} and Eu^{3+}at 245 nm, $Gd_{1.88}Eu_{0.12}O_3$ exhibited a dominant red emission peak at 611 nm attributed to the $^5D_0 \rightarrow {}^7F_2$ electric dipole transition, and the intensity of the dominant red emission peak increased consistently with the average crystallite size of $Gd_{1.88}Eu_{0.12}O_3$.

(3) The dispersion property of Eu^{3+} ions doped in the host Gd_2O_3 was thought to be improved by using CP method, which could lead to the relatively high PL red

emission intensity achieved for the $Gd_{1.88}Eu_{0.12}O_3$ at the Li^+ doping from 0 to 8 mol%.

(4) The Li^+-doped cubic $Gd_{1.88}Eu_{0.12}O_3$ phosphor mounted on a VFD showed room-temperature red CL at an anode voltage of 50 V, and the maximum luminance intensity for the CL red emission was achieved for 8 mol% Li^+-doped $Gd_{1.88}Eu_{0.12}O_3$ synthesized by SS method.

(5) Under the present VFD operation condition at the low excitation voltage, the penetration depth of electrons into the $Gd_{1.88}Eu_{0.12}O_3$ was considered to be extremely shallow. Therefore, it could be essential for enhancing the luminance intensity to maintain a sufficient surface area of the $Gd_{1.88}Eu_{0.12}O_3$ mounted on a VFD. As a result, the SSA value of approximately $0.8 m^2/g$ was suggested as a lower limit required for improving CL emission intensity.

References

[1] X. Wang, Z. Zhao, Q. Wu, Y. Li, C. Wang, A. Mao and Y. Wang, Roy. Soc. Chem., **44**, 11057-11066 (2015).

[2] J. C. Park, H. K. Moon, D. K. Kim, S. H. Byeon, B. C. Kim and K. S. Suh, Appl. Phys. Lett., **77**, 2162-2164 (2000).

[3] H. Li, Z. Wang and J. Hao, Mater. Sci. Eng., **1**, 1-7 (2009).

[4] J. Ballato, J. S. Lewis and P. H. Holloway, Mater. Res. Soc. Bull., **24**, 51-56 (1999).

[5] J. M. Fitz-Gerald, T. A. Trottier, R. K. Singh and P. H. Hollowary, Appl. Phys. Lett., **72**, 1838-1840 (1998).

[6] K. Tanaka, S. Okamoto, H. Kominami, Y. Nakanishi, X. Du and A. Yoshikawa, J. Appl. Phys., **92**, 834-837 (2002).

[7] P. Guo, F. Zhao, G. Li, F. Liao, S. Tian and X. Jing, J. Lumin., **105**, 61-67 (2003).

[8] H. C. Swart, T. A. Trottier, J. S. Sebastian, S. L. Jones and P. H. Holloway, J. Appl. Phys., **83**, 4578-4583 (1998).

[9] C. C. Lin, K. M. Lin and Y. Y. Li, J. Lumin., **126**, 795-799 (2007).

[10] M. Hong, J. Kwo, A. R. Kortan, J. P. Mannaerts and A. M. Sergent, Science, **283**, 1897-1900 (1999).

[11] X. Wang, X. Sun, D. Yu, B. Zou and Y. Li, Adv. Mat., **15**, 1442-1445 (2003).

[12] H. Xiao, P. Li, F. Jia and L. Zhang, J. Phys. Chem. C, **113**, 21034-21041 (2009).

[13] J. Li, Q. Zhu, X. Li, X. S and Y. Sakka, Acta Materialia, **59**, 3688-3696 (2011).

[14] R. Kumar, S. hat, K. Ikeda and K. Gopchandran, Ceramics International, **40**, 2915-2926 (2014).

[15] L. Liu, E. Ma, R. Li, G. Liu and X. Chen, Nanotechnology, **18**, 015403-015408 (2007).

[16] K. Lin and Y. Li, Nanotechnology, **17**, 4048-4052 (2006).

[17] A. M. Pires, M. R. Davolos, C. O. Paiva-Santos, E. B. Stucchi and J. Flor, J. Solid State Chem., **171**, 420-423 (2003).

[18] M. Ko, J. Park, D. Kim and S. Byeon, J. Lumin., **104**, 215-221 (2003).

[19] R. Tamrakar, D. Bisen and N. Brahme, J. Bio. Chem. Lumin., **10**, 2913-2921 (2015).

[20] J. Yang, C. Li, Z. Cheng, X. Zhang, Z. Quan, C. Zhang and J. Lin, J. Phys. Chem. C, **111**, 18148-18154 (2007).

[21] G. Rajan and K. G. Gopchandran, App. Surf. Sci., **255**, 9112-9123 (2009).

[22] S. H. Shin, J. H. Kang, D. Y. Jeon and D. S. Zang, J. Lumin., **114**, 275-280 (2005).

[23] Y. Kang, Y. Shimokawa, Y. Ishihara, L. Miao, S. Tanemura and Y. Iwamoto, J. Lumin., **166**, 238-243 (2015).

[24] F. Wang, Y. Han, C. Lim, Y. Lu, J. Wang and J. Xu, Nature, **463**, 1061-1065 (2010).

[25] Y. Wang, S. Lau, H. Lee, S. Yu, B. Tay, X. Zhang and H. Hng, J. App. Phys., **94**, 354-358 (2003).

[26] T. Kano, "Luminescence centers of rare-earth ions," Phosphor Handbook, pp. 192 (1998).

[27] M. Nogami, T. Enomoto and T. Hayakawa, J. Lumin., **97**, 147-152 (2002).

[28] J. X. Wan, Z. H. Wang, X. Y. Chen, L. Mu and Y. T. Qian, J. Cryst. Growth, **284**, 538-543 (2005).

[29] K. Y. Jung and K. H. Han, Electrochem. Solid-State Lett., **8**, H17-H20 (2005).

[30] J. Yang, X. M. Liu, C. X. Li, Z. W. Quan, D. Y. Kong and J. Lin, J. Cryst. Growth, **303**, 480-486 (2007).

[31] C. Feldman, Phys. Rev. **117**, 455-459 (1960).

[32] X. Liu, C. Lin, Y. Luo and J. Lin, J. Electrochem. Soc. **154**, J21-J27 (2007).

CHAPTER 4: Relationship between Eu^{3+} substitution sites and photoluminescence properties of $SrIn_2O_4:Eu^{3+}$ spinel phosphors

4.1. Introduction

For the past dedicate, because of the good thermal and chemical stability, rare earth ion-doped oxide phosphors have attracted much attention as they can be used in various type of display devices, solid-state lasers, medical devices, lighting apparatus and so on [1-4]. Furthermore, the white light-emitting diodes (white LEDs) have been expected as the next generation solid-state lighting sources to replace the conventional incandescent and fluorescent lamps. The white LEDs become more and more popular owing to the favorable properties like the excellent luminescent characteristics, high energy conversion efficiency, low cost and long operation time [5, 6].

The white LEDs have been fabricated by covering blue LED chips with a yellow emitting phosphor, cerium-doped yttrium aluminum garnet (YAG:Ce^{3+}) [7, 8]. However, the white LEDs fabricated in this way have drawbacks such as the low color rendering index (less than 80) and high correlated color temperature (higher than 7000 K), which restricts their wide range of applications. As one of promising approaches to overcome the drawbacks, ultraviolet (UV) or near-UV LED chip excited tri-color (blue, green and red) phosphors have been considered and studied as a better combination for white LEDs which can offer a color rendering index higher than 90 [9, 10].

However, commercially available red-emitting phosphors are sulfides such as (Ca, Sr)S:Eu^{3+} and $Y_2O_2S:Eu^{3+}$ [11]. Due to the lower chemical stability, sulfide-based phosphors degrade in the white LED devices during operation. Therefore, it is important to develop efficient novel phosphors, particularly red-emitting phosphors that can be excited efficiently under UV or near-UV irradiation. As one of the famous red emitters in the rare earth ion-doped materials, Eu^{3+} ion primarily presents highly efficient emissions due to the large energy gap between the emitting state $^5D_0$ and the excited states ^7F_J (J=0-5) for the contribution of the extraordinary red composition. In addition to the excellent chemical stability, wide

band gap semiconducting oxides with active Eu^{3+} ion are promising red color phosphors [12, 13]. Among these oxide phosphors, indium compounds such as $CaIn_2O_4$ [14-20] and $SrIn_2O_4$ [21-29] have been reported as excellent host materials for rare earth metal cations doped phosphors. $CaIn_2O_4$ is a kind of semiconductor with a reported bandgap of 3.9 eV, and belongs to ordered $CaFe_2O_4$ structures with the *Pca*21 or *Pbcm* space group and the lattice parameters of a=0.970 nm, b=1.130 nm and c=0.321 nm for *Z*=4 [30]. Several dopant cations such as Tb^{3+} [14-16] and Pr^{3+} [16] for green emission, Dy^{3+} [16] for blue-white emission and Eu^{3+} for white [17, 18], yellow [18], orange [18], reddish orange [20] and red [18, 19] emissions under ultraviolet (UV) and/or vacuum-ultraviolet (VUV) excitation have been investigated for developing field emission displays (FEDs), cathode ray tube display (CRTs) and white-LEDs. The chemical composition of these phosphors were mainly designed and synthesized to occupying Ca^{2+} sites with the dopant cation in the host $CaIn_2O_4$. For tuning the emission colors except for red emission, the dopant concentrations in these phosphors were very low and in the range of 0.12 to 0.32 mol%, while the intense red emission was achieved for 15 mol% Eu^{3+} doped $CaIn_2O_4$ with 5 mol% Sm^{3+} co-doping ($Ca_{0.8}In_2O_4$:0.15Eu^{3+}, 0.05Sm^{3+}) [19].

Another indium compound, $SrIn_2O_4$ is also a semiconductor with a reported bandgap of 3.6 eV, and the red-emitting $SrIn_2O_4$:Eu^{3+} has attracted much attention for application to white LEDs, because $SrIn_2O_4$ has a strong absorption band at 396 nm, which perfectly matches with the emission spectrum of GaN-based LED chips [21-23]. The crystal structure of $SrIn_2O_4$ is an orthorhombic $CaFe_2O_4$-type structure with Pnam (D_{2h}^{16}) space group and the lattice parameters of a=0.981 nm, b=1.145 nm and c=0.327 nm for *Z*=4 [24]. In the structure of $SrIn_2O_4$ (Fig. 4-1), two kinds of distorted InO_6 octahedra are connected to form a network by sharing edges and corners, and the In^{3+} ions are in six coordination with the ionic radii of 0.080 nm [25, 26]. On the other hand, Sr^{2+} ions located in the middle of the formed pentagonal prism tunnel are in eight coordination with the ionic radii of 0.126 nm [24]. Baszczuk *et al.* [26] reported that Eu ions can occupy all the Sr^{2+} and two different In^{3+} sites in the host $SrIn_2O_4$. From the results of luminescence spectroscopic analyses for

$SrIn_2O_4:Eu^{3+}$, they concluded that Eu^{3+} ions occupy two different In^{3+} sites, while a part of Eu^{3+} ions in the host $SrIn_2O_4$ could be reduced to Eu^{2+} even under non-reducing atmosphere, and the in-situ produced Eu^{2+} could occupy the Sr^{2+} site.

If dopant Eu^{3+} ion preferentially occupies the Sr^{2+} site in the host $SrIn_2O_4$, the resulting charge imbalance may be compensated by formation of Sr^{2+} vacancies, which would increase the nonradiative process and result in the reduction of luminescence intensity. Because the luminescent property of phosphor arises from the complex interaction among host structure, activators, defects and interfaces. Wang *et al.* [27] reported that alkali ions are effective as a co-dopant to compensate the charge imbalance caused by the Eu^{3+} substitution at the Sr^{2+} site in the host $SrIn_2O_4$, and a remarkable improvement in the PL emission intensity was achieved for $Sr_{1-x}In_2O_4:xEu^{3+}, xNa^{+}$ (x=0.1).

However, to our knowledge, there is no systematic study on the PL red-emitting properties related to the dominant Eu^{3+} occupying site, and the total concentration of Eu^{3+} ions which may occupy all the Sr^{2+} and In^{3+} sites in the host $SrIn_2O_4$. In this work, we have investigated the fabrication and photoluminescence (PL) properties of $SrIn_2O_4:Eu^{3+}$ phosphors. The relationship between the PL emission peaks due to the dopant Eu^{3+}, the site substituted by the Eu^{3+}, oxidation state of the doped Eu^{3+} and the critical Eu^{3+} concentration in the host $SrIn_2O_4$ lattice were studied. Moreover, the temperature quenching effect is also measured from room temperature to 227 ℃ (500 K), and the results were discussed from a viewpoint to develop an efficient red-emitting phosphor for white LED applications.

4.2. Experimental procedures

Eu^{3+}-doped $SrIn_2O_4$ phosphors were synthesized by the solid solution method following the procedure reported by Lakshminarasimhan *et al.* [28]. Strontium carbonate ($SrCO_3$), indium oxide (In_2O_3) and europium oxide (Eu_2O_3) were used as starting materials. All the powders were purchased from Mitsuwa Chemical Company,

Japan (99.99% purity). In a typical synthesis, appropriate amounts of the three starting powders (totally about 2 g) were mixed and then stirred in the 5 mL ethanol for 10 min. The mixed powder was placed into a drying furnace at 100 ℃ for 5 min to remove the ethanol. The dried powder was heat-treated at 1400 ℃ in air for 4 h. The chemical compositions of the Eu^{3+}-doped $SrIn_2O_4$ investigated in this study were shown in Table 4-1.

Table 4-1. Chemical composition of $SrIn_2O_4:Eu^{3+}$ phosphors investigated in this study.

Sample				Molar ratio of starting materials		
Formula	x	y	Composition	$SrCO_3$	In_2O_3	Eu_2O_3
$SrIn_{2-x}O_4:xEu^{3+}$	0.005	-	$Sr_{1.00}In_{1.995}O_4:0.005Eu^{3+}$	1	0.9975	0.0025
	0.01	-	$Sr_{1.00}In_{1.99}O_4:0.01Eu^{3+}$	1	0.995	0.005
	0.10	-	$Sr_{1.00}In_{1.90}O_4:0.10Eu^{3+}$	1	0.95	0.05
	0.15	-	$Sr_{1.00}In_{1.85}O_4:0.15Eu^{3+}$	1	0.925	0.075
	0.20	-	$Sr_{1.00}In_{1.80}O_4:0.20Eu^{3+}$	1	0.9	0.1
	0.25	-	$Sr_{1.00}In_{1.75}O_4:0.25Eu^{3+}$	1	0.875	0.125
	0.30	-	$Sr_{1.00}In_{1.70}O_4:0.30Eu^{3+}$	1	0.85	0.15
$Sr_{1-y}In_{2-x}O_4:0.1Eu^{3+}$ (x + y = 0.1)	0.09	0.01	$Sr_{0.99}In_{1.91}O_4:0.10Eu^{3+}$	0.99	0.955	0.05
	0.07	0.03	$Sr_{0.97}In_{1.93}O_4:0.10Eu^{3+}$	0.97	0.965	0.05
	0.05	0.05	$Sr_{0.95}In_{1.95}O_4:0.10Eu^{3+}$	0.95	0.975	0.05
	0.03	0.07	$Sr_{0.93}In_{1.97}O_4:0.10Eu^{3+}$	0.93	0.985	0.05
	0.01	0.09	$Sr_{0.91}In_{1.99}O_4:0.10Eu^{3+}$	0.91	0.995	0.05
	-	0.10	$Sr_{0.90}In_{2.00}O_4:0.10Eu^{3+}$	0.90	1	0.05
$Sr_{1-y}In_{1.75}O_4:(y+0.25)Eu^{3+}$ (x = 0.25)	0.25	0.02	$Sr_{0.98}In_{1.75}O_4:0.27Eu^{3+}$	0.98	0.875	0.135
	0.25	0.04	$Sr_{0.96}In_{1.75}O_4:0.29Eu^{3+}$	0.96	0.875	0.145
	0.25	0.06	$Sr_{0.94}In_{1.75}O_4:0.31Eu^{3+}$	0.94	0.875	0.155
	0.25	0.08	$Sr_{0.92}In_{1.75}O_4:0.33Eu^{3+}$	0.92	0.875	0.165
	0.25	0.10	$Sr_{0.90}In_{1.75}O_4:0.35Eu^{3+}$	0.90	0.875	0.175

Room temperature X-ray diffraction (XRD; X`pert Pro α1, Philips) analysis was performed on the heat-treated samples using Cu Kα radiation (λ=0.15405 nm). The morphology of the heat-treated samples was observed using scanning electron microscopy (SEM; JSN-6360LV, JEOL) at 25 kV acceleration voltages. Evaluation of oxidation state for the doped-Eu ions was performed by measurements of X-ray

absorption near edge structure (XANES) spectra at the Eu LIII absorption edge with X-ray absorption spectrometer (Rigaku, R-XAS Looper). The obtained XANES spectra were analyzed by the software (Rigaku, REX2000).

PL excitation and emission spectra were recorded at room temperature using a spectrophotometer (F-7000, Hitachi) with a 150 W Xenon lamp as the excitation source. The temperature dependence of the red PL of the phosphor was evaluated under the excitation at 393 nm.

4.3. Results and discussion

4.3.1. Crystalline phases of 1400 ºC heat-treated samples

The XRD patterns for $SrIn_{2-x}O_4:xEu^{3+}$ (x=0.005, 0.01 and 0.1) and those for $Sr_{1-y}In_{2-(0.1-y)}O_4:0.1Eu^{3+}$ (y=0.01, 0.03, 0.05, 0.07, 0.09 and 0.1) are shown in Figs. 4-2 (a) and 4-2 (b), respectively. The diffraction peaks detected for each sample except for $Sr_{0.9}In_2O_4:0.1Eu^{3+}$ (y=0.1 in Fig. 4-2 (b)) were identical to those of the standard powder diffraction file for orthorhombic $SrIn_2O_4$ (JCPDS No. 01-072-0801, space group: Pnam (D_{2h}^{16})). As previously reported [26], no systematic shifting of XRD diffraction peaks with increasing x was observed for $SrIn_{2-x}O_4:Eu^{3+}$ (x=0.005 and 0.01 in Fig. 4-2 (a)), which is due to that variation of the unit cell by small amount of Eu^{3+} dopant is within the detection limit of the equipment used in this study. The lattice parameters determined for these two compositions were a = ~ 0.982 nm, b = ~ 0.1148 nm, and c = ~ 0.327 nm. When x was increased to 0.1(x=0.1 in Fig. 4-2 (a)), the lattice parameter in the c axis almost unchanged, while those in the a and b axes slightly increased to ~0.985 nm and ~0.115 nm, respectively, which indicates that doped Eu^{3+} (0.095 nm) occupied In^{3+} (0.080 nm) site as designed.

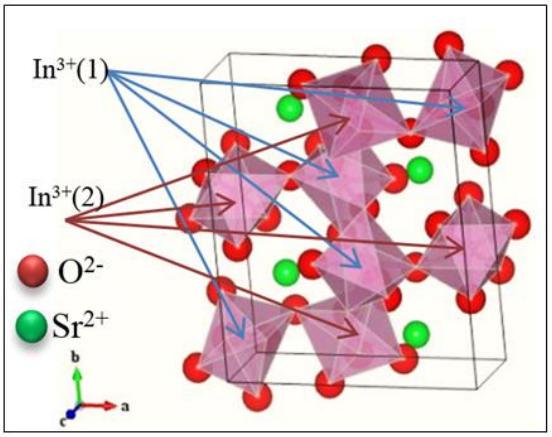

Fig. 4-1. Crystal structure of orthorhombic $SrIn_2O_4$.

On the other hand, $Sr_{0.9}In_2O_4$:0.1Eu^{3+} exhibited additional diffraction peaks assigned to indium oxide (In_2O_3, JCPDS card of No. 00-044-1087), while the rest of five compositions exhibited $SrIn_2O_4$ single phase without formation of strontium oxide (SrO) and other phases of Eu^{3+} ion, thus the doped Eu^{3+} ion was well dissolved into the $SrIn_2O_4$ host lattice. These results indicate that Eu^{3+} ion principally occupies In^{3+} site, then occupies Sr^{2+} site as a secondary substitution site in the host $SrIn_2O_4$. Since the size difference between In^{3+} (0.080 nm) and Eu^{3+} (0.095 nm) in six coordination is 18.8%, which is rather larger than that between Sr^{2+} (0.126 nm) and Eu^{3+} (0.107 nm) in eight coordination (15.1%), this order is thought to be governed by the valence difference between Sr^{2+} and Eu^{3+}, which leads to the intrinsic Eu^{3+} content restriction in the host $SrIn_2O_4$ [22, 27].

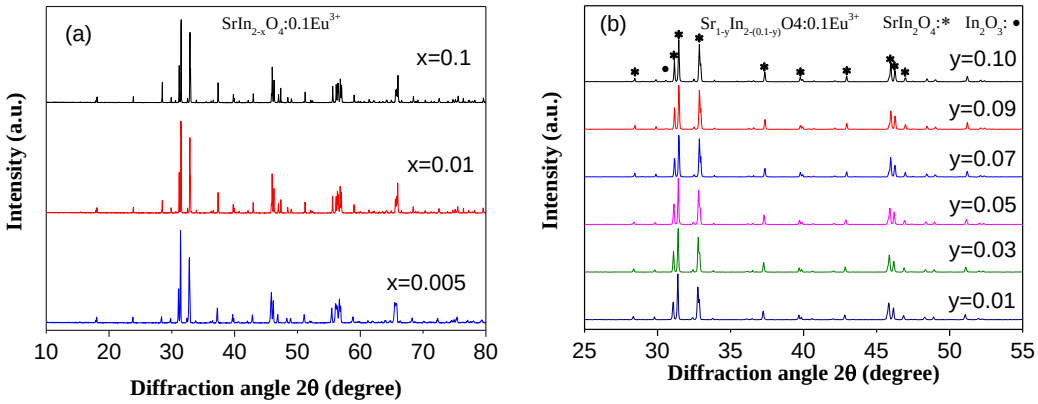

Fig. 4-2. The XRD patterns for (a) $SrIn_{2-x}O_4$:0.1Eu^{3+} (x=0.005, 0.01, 0.1) and (b) $Sr_{1-y}In_{2-(0.1-y)}O_4$:0.1$Eu^{3+}$ (y =0.01, 0.03, 0.05, 0.07, 0.09 and 0.1).

4.3.2. PL properties

As shown in Fig. 4-1, there are one Sr^{2+} site and two different In^{3+} sites in the host $SrIn_2O_4$, the dopant Eu^{3+} ion in the five compositions of Sr_{1-y} $In_{2-(0.1-y)}O_4$:$0.1Eu^{3+}$ (y=0.01, 0.03, 0.05, 0.07, 0.09) can be substituted in all of them. Then, their PL properties were further studied. As a typical result, Fig. 4-3 (a) presents the excitation spectrum ($\lambda_{em.}$= 611 nm) and emission spectrum ($\lambda_{ex.}$= 393 nm) for $Sr_{0.95}In_{1.95}O_4$:$0.1Eu^{3+}$ (y=0.05). In the excitation spectrum, a broad peak at around 345 nm can be observed and is ascribed to the band gap transition of $SrIn_2O_4$ host lattice [29]. The intense excitation peaks at 393 and 464 nm can be attributed to the $^7F_0 \rightarrow {}^5L_6$ and the $^7F_0 \rightarrow {}^5D_2$ excitations, respectively [26]. In addition to its relatively higher intensity, the excitation peak wavelength of 393 nm well matches with the emission spectrum of GaN-based LEDs, which offers a possibility for white LED applications. Thus, the excitation at 393 nm was employed for evaluating PL emission properties of the phosphors investigated in this study.

Upon an excitation with 393 nm, the emission spectrum exhibits several peaks due to the $^5D_0 \rightarrow {}^7F_J$ (J=0-4) transitions of Eu^{3+} over the range of 570-730 nm, and the main emission attributed to the $^5D_0 \rightarrow {}^7F_2$ electric dipole transition are observed as three peaks at 611, 616 and 623 nm (Fig. 4-3 (b)). Thus, $Sr_{0.95}In_{1.95}O_4$:$0.1Eu^3$ exhibits red emission.

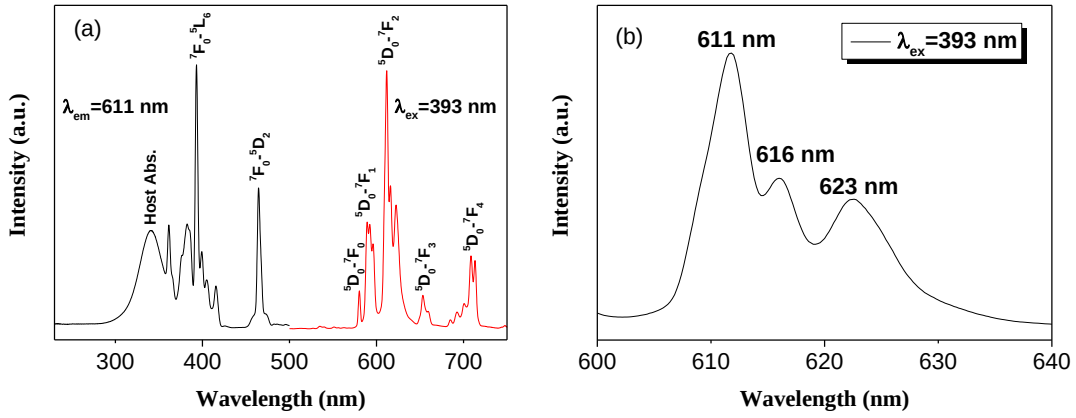

Fig. 4-3. PL excitation spectrum ($\lambda_{em.}$ = 611 nm) and emission spectrum ($\lambda_{ex.}$ = 393 nm) for $Sr_{0.95}In_{1.95}O_4$:$0.1Eu^{3+}$ ($Sr_{1-y}In_{2-(0.1-y)}O_4$:$0.1Eu^{3+}$, y=0.05).

PL emission spectra ($\lambda_{ex.}$ = 393 nm) for $Sr_{1-y}In_{2-(0.1-y)}O_4$:0.1$Eu^{3+}$ phosphors (y=0, 0.01, 0.03, 0.05, 0.07, 0.09 and 0.10) are shown in Fig. 4-4 (a). All the samples exhibited dominant red emission peaks at 611-623 nm. These spectra were curve-fitted and the relative intensities for each emission peak centered at the 611, 616 and 623 nm were evaluated and are plotted in Fig. 4-4 (b) as a function of y, *i.e.* amount of Eu^{3+} at Sr^{2+} site ($Sr_{1-y}In_{2-(0.1-y)}O_4$:0.1$Eu^{3+}$). Initially at y=0, the relative peak intensity was in the order of 611 nm > 623 nm > 616 nm. However, the intensity at 616 nm significantly increased with increasing y, and became highest at y= 0.05. Then, the intensity slightly increased above y=0.05 to reach a maximum at y=0.09. Conversely, the relative peak intensities at 611 and 623 nm decreased with increasing y, *i.e.* with decreasing amount of Eu^{3+} ions at In^{3+} site. At y=0.1, intensities of the three peaks were lowest, which could be due to the secondary phase formation of In_2O_3 as shown in Fig. 4-1 (b). These results reveal that the emission peak intensity at 616 nm largely depends on the amount of Eu^{3+} ion at Sr^{2+} site, while those at 611 and 623 nm are dominantly governed by the amount of Eu^{3+} ion at the two different In^{3+} sites.

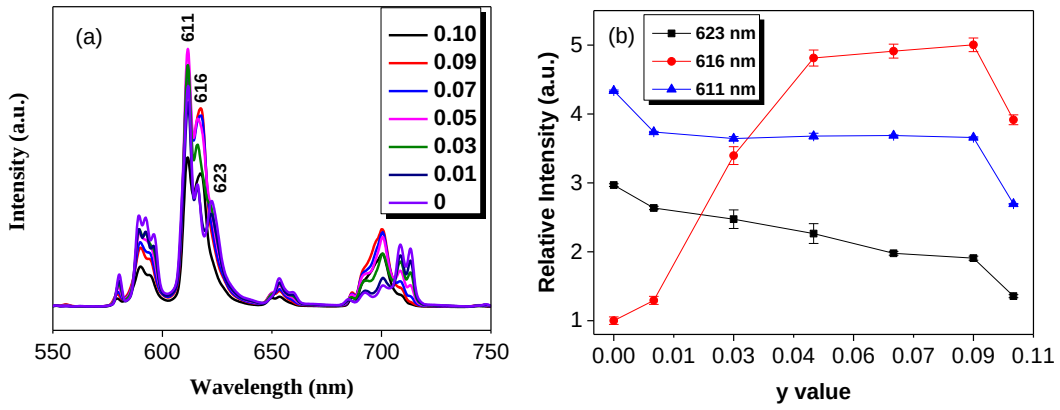

Fig. 4-4. (a) PL emission spectra ($\lambda_{ex.}$ = 393 nm) for $Sr_{1-y}In_{2-(0.1-y)}O_4$:0.1$Eu^{3+}$ phosphors (y=0, 0.01, 0.03, 0.05, 0.07, 0.09 and 0.10), and (b) variation of relative emission peak intensities at 611, 616, 623 nm in the spectra shown in (a).

To investigate the possibility of the PL emission ascribed to Eu^{3+} ion at the two different In^{3+} sites, further analysis of the PL emission spectrum ($\lambda_{ex.}$ = 393 nm) was performed on $SrIn_{1.99}O_4$:0.01Eu^{3+}, since no SrO diffraction peaks was found in the

XRD diffraction pattern for this composition and the doped Eu^{3+} ions was thought to mainly occupy the In^{3+} sites. As shown in Fig. 4-5, only the characteristic f-f transition peaks of Eu^{3+} can be seen in the spectrum. There are several PL emission peaks due to the large energy gap between the emitting state $^5D_0$ and the excited states ^7F_J (J=0-2) which contribute the red emission. The details of the PL emission peaks are summarized and shown in Table 4-2.

Table 4-2. PL emission peaks due to Eu^{3+} measured for $SrIn_{1.99}O_4:0.01Eu^{3+}$ under excitation at 393 nm.

Transition	Peak (nm)	Transition	Peak (nm)
$^5D_0 \rightarrow {}^7F_0$	578	$^5D_0 \rightarrow {}^7F_2$	611
	584		614
$^5D_0 \rightarrow {}^7F_1$	586		616
	590		618
	592		624
	595		627

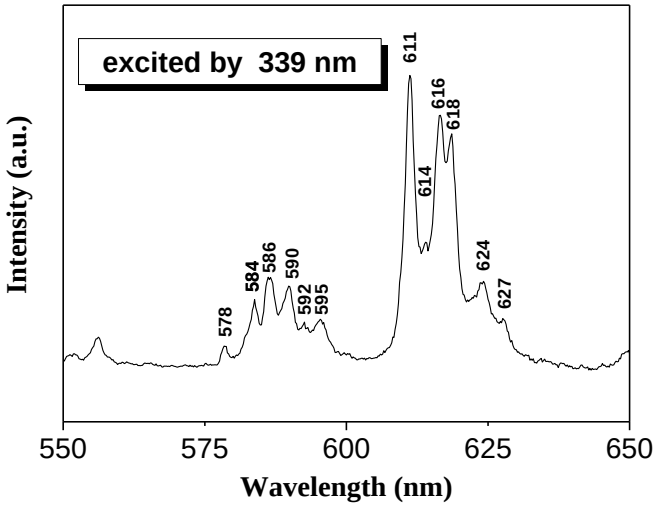

Fig. 4-5. PL emission spectrum ($\lambda_{ex.}$ = 393 nm) for $SrIn_{1.99}O_4:0.01Eu^{3+}$.

When the rare earth (RE) ion is incorporated in a host material the energy level of the RE ion is generally splitted into number of sublevels due to the ligand field/ crystal field. These sublevels are known as the Stark sublevels, and the maximum

number of the f-f transition peaks due to RE ion can be given as 2J+1 (where J is the electronic angular momentum). Therefore, there should be only one peak for the $^7F_0$ level, while there are two different peaks at 578 and 584 nm due to the $^5D_0 \rightarrow {}^7F_0$ transition (Table 4-2). It is also well known that the maximum numbers of the Stark sublevels depend on the symmetry of the crystal field surrounding RE ion [31, 32]. As shown in Fig. 4-5, the high emission intensity achieved by the hypersensitive $^5D_0$ to $^7F_2$ transition reveals that the point symmetry of Eu^{3+} ion at In^{3+} site is low. Therefore, there should be less than three and five peaks for the splitting of $^7F_1$ and $^7F_2$ levels, respectively. However, as shown in Table 4-2, there are four and six peaks attributed to the $^5D_0 \rightarrow {}^7F_1$ and the $^5D_0 \rightarrow {}^7F_2$ transitions, respectively. These results demonstrate that the dopant Eu^{3+} ion randomly occupied the two different In^{3+} sites in the host $SrIn_2O_4$ investigated in this study.

4.3.3. Optimization of PL red emission intensity

To improve the performance as a red-emitting phosphor, optimization of the dopant Eu^{3+} ion concentration in the host $SrIn_2O_4$ lattice was further investigated according to the following strategy based on the results obtained shown above: (1) optimizing total amount of Eu^{3+} ion at the two different In^{3+} sites, then (2) optimizing the amount of Eu^{3+} ion at Sr^{2+} site for the $SrIn_2O_4$ with the optimized amount of Eu^{3+} ions occupying the two In^{3+} sites. Figure 4-6 shows PL emission spectra for $SrIn_{2-x}O_4:xEu^{3+}$ (x = 0.1, 0.15, 0.2, 0.25 and 0.3) upon an excitation at 393 nm. Among the three dominant red emission peaks at 611, 616 and 623 nm attributed to the $^5D_0 \rightarrow {}^7F_2$ transition, the most intensive one at 611 nm was selected, and the inset shows variation of the relative peak intensity at 611 nm. The intensity of the red emission peaks increased consistently with Eu^{3+} concentration and reached a maximum at x=0.25, then became lowest at x=0.3. The XRD analysis revealed that all the $SrIn_{2-x}O_4:xEu^{3+}$ phosphors were composed of $SrIn_2O_4$ single phase, and the degradation at x=0.3 was thought to be due to the concentration quenching.

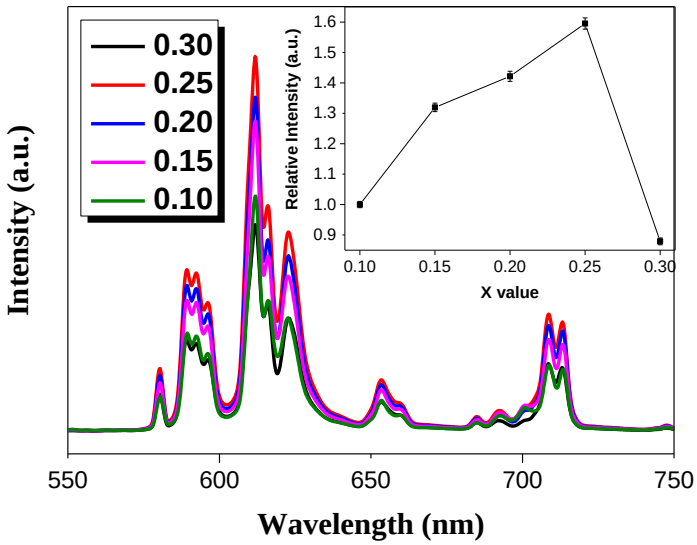

Fig. 4-6. PL emission spectra excited at 393 nm for $SrIn_{2-x}O_4:xEu^{3+}$ with different amount of Eu^{3+} (x = 0.1, 0.15, 0.2, 0.25 and 0.3). Inset shows relative intensity of the emission peak at 611 nm as a function of Eu^{3+} content.

Then, a series of $Sr_{1-y}In_{1.75}O_4:(y+0.25)Eu^{3+}$ (y=0.02, 0.04, 0.06, 0.08 and 0.10) were synthesized and characterized by comparing with $SrIn_{1.75}O_4:0.25Eu^{3+}$. As shown in Fig. 4-7, all the phosphors exhibited the same XRD pattern identical to orthorhombic $SrIn_2O_4$ phase. As typical morphological features, SEM images of $Sr_{1-y}In_{1.75}:(y+0.25)Eu^{3+}$ (y=0, 0.04, 0.08 and 0.1) are shown in Fig. 4-8. All the phosphors exhibited a similar microstructural feature, and presented crystallites having a size range of about 1 to 4 μm.

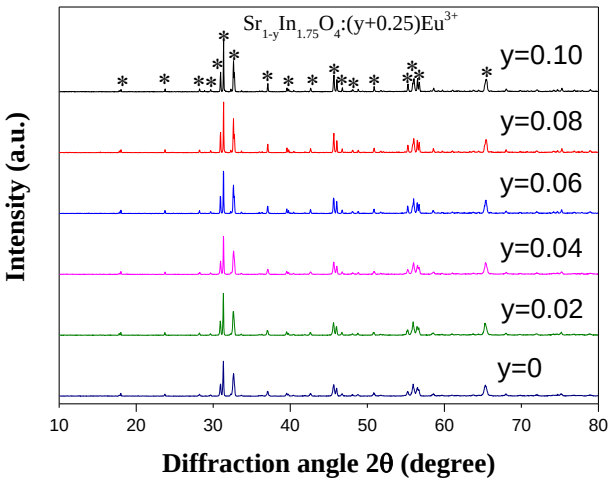

Fig. 4-7. The XRD patterns for $Sr_{1-y}In_{1.75}O_4:(y+0.25)Eu^{3+}$ (*: Orthorhombic $SrIn_2O_4$).

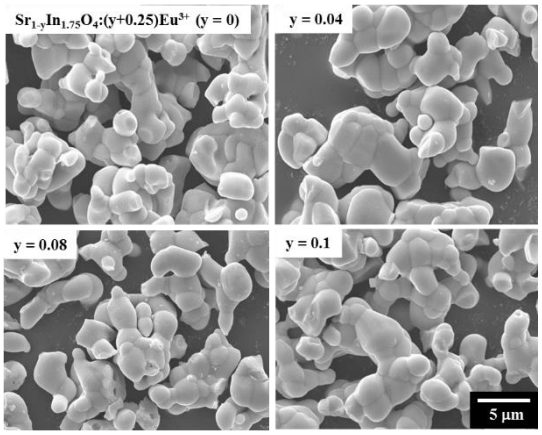

Fig. 4-8. SEM images of $Sr_{1-y}In_{1.75}O_4$:(y+0.25)Eu^{3+} (y=0, 0.04, 0.08 and 0.1).

Figure 4-9 (a) illustrates PL emission spectra for the $Sr_{1-y}In_{1.75}O_4$:(y+0.25)Eu^{3+} phosphors (y=0, 0.02, 0.04, 0.06, 0.08 and 0.10) upon an excitation at 393 nm. The variations of relative peak intensities at 611, 616 and 623 nm, and the resulting red emission intensity evaluated as the total intensity of the three emission peaks due to the $^5D_0 \rightarrow {}^7F_2$ transition are shown in Figs. 4-9 (b) and 4-9 (c), respectively. In this optimization study, the Eu^{3+} concentration at the In^{3+} site was optimized and fixed as 25% prior to increasing the amount of Eu^{3+} at the Sr^{2+} site, and the relative peak intensities at 611, 616 and 623 nm were found to keep the initial intensity order (611 nm > 623 nm > 616 nm) at all the compositions (Fig. 4-9 (b)). The relative peak intensity at 616 nm increased consistently with the amount of Eu^{3+} ion-doping, and reached a maximum at y=0.08 to 0.1, while those at 611 and 623 nm increased to reach a maximum at y=0.08, then apparently decreased at y=0.1 (Fig. 4-9 (b)). As a result, the maximum red emission intensity ascribed to the $^5D_0 \rightarrow {}^7F_2$ transition was achieved for $Sr_{0.92}In_{1.75}O_4$:0.33Eu^{3+} (y=0.08). This intensity was 2.2 times higher than that of $SrIn_{1.75}O_4$:0.25Eu^{3+} (y=0) (Fig. 4-9 (c)).

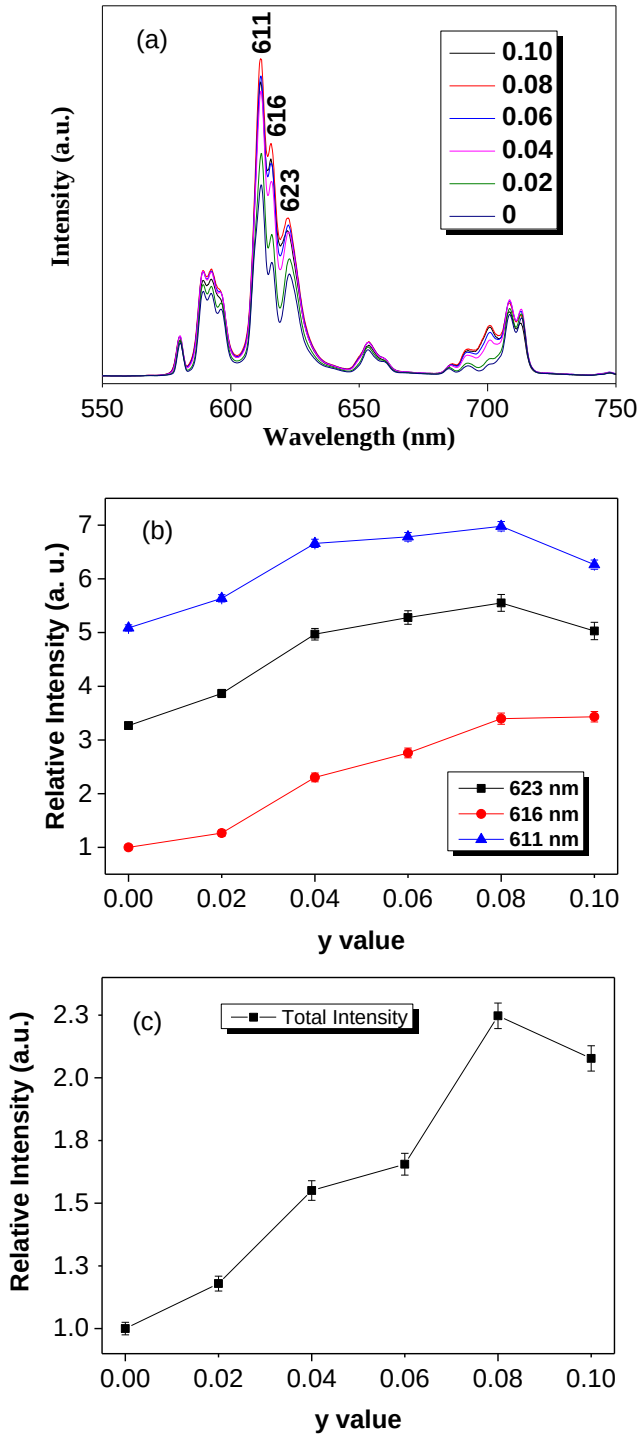

Fig. 4-9. PL emission properties of $Sr_{1-y}In_{1.75}O_4$:(y+0.25)Eu^{3+}. (a) PL spectra exited at 393 nm. Composition dependences of (b) relative emission peak intensities at 611, 616 and 623 nm and (c) the total emission intensity.

The oxidation state of the doped Eu ions was investigated by the XANES spectroscopy. The spectrum obtained for $Sr_{0.92}In_{1.75}O_4$:0.33Eu^{3+} is compared with that for the reference sample of Eu_2O_3 and shown in Fig. 4-10. Both of the two samples

exhibit a single band peak centered at 6988 eV assigned to Eu^{3+} [33], and thus the oxidation state of the Eu ions in the $Sr_{0.92}In_{1.75}O_4:0.33Eu^{3+}$ synthesized in this study was determined as trivalent.

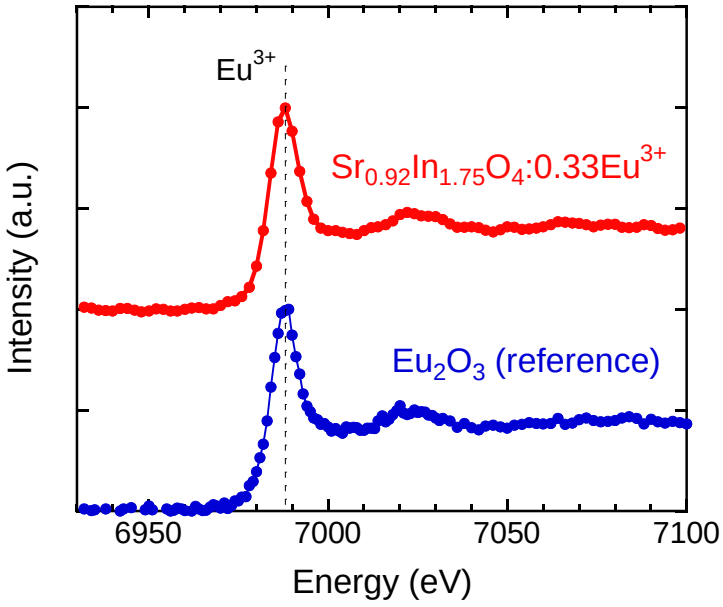

Fig. 4-10. XANES spectra for $Sr_{0.92}In_{1.75}O_4:0.33Eu^{3+}$ and reference sample of Eu_2O_3.

The emission peak intensity at 616 nm increased associated with a simultaneous increase in the emission peak intensities at 611 and 623 nm, which could be due to the preferential Eu^{3+} substitution at In^{3+} sites as discussed above. Thus, a part of the additionally doped Eu^{3+} ion occupied the In^{3+} sites, and the exact Eu^{3+} ion concentration at Sr^{2+} site in the $Sr_{0.92}In_{1.75}O_4:0.33Eu^{3+}$ could be less than 8 mol%.

When the dopant Eu^{3+} ion occupies Sr^{2+} site, the resulting charge imbalance may be compensated by formation of Sr^{2+} vacancies as follows:

$$Eu_2O_3 \rightarrow 2Eu^{\bullet}_{Sr} + 3O^{\times}_{O} + V''_{Sr}{}^{\bullet} \qquad (1)$$

As previously discussed for Na^+-codoped $Sr_{1-x}In_2O_4:xEu^{3+}$ phosphors ($Sr_{1-x-x}In_2O_4:xEu^{3+},xNa^+$) [27], under such a low Eu^{3+} concentration below 8 mol%, the degree of charge imbalance formed by the Eu^{3+} substitution at Sr^{2+} site could be low. Thus, the red emission intensity successfully increased without a serious

reduction in the emission intensity caused by the formation of Sr^{2+} vacancies.

The optimized total amount of dopant Eu^{3+} ion in the host $SrIn_2O_4$ was determined to be 0.33, above which the red emission intensity decreased due to the concentration quenching. Since the concentration quenching is caused by energy transfer from one activator to another one, there is a critical energy transfer distance (R_c). In oxide phosphors, the R_c can be estimated by the following equation [34, 35]:

$$R_c = 2\left(\frac{3V}{4\pi X_c N}\right)^{1/3} \qquad (2)$$

where V is the volume of the unit cell, X_c is the critical concentration of the dopant ions and N is the number of host cation in the unit cell. By using appropriate values of V (0.376 nm^3), X_c (0.33) and N (4) [24, 36], the critical energy transfer distance of Eu^{3+} ion in the $Sr_{0.92}In_{1.75}O_4$:$0.33Eu^{3+}$ (R_c) is determined to be 0.817 nm.

Park *et al*. [37] reported that the melilite structure $CaYAl_3O_7$ has a high Eu^{3+} concentration without concentration quenching compared to other host materials, and the optimized Eu^{3+} ion concentration and the R_c for the red-emitting $CaY_{1-x}Al_3O_7$:xEu^{3+} were determined to be approximately 35 mol% (x=0.35) and 0.9 nm, respectively. The values obtained in this study are compatible with those reported for the $CaY_{1-x}Al_3O_7$:xEu^{3+}, and relatively high dopant Eu^{3+} ion concentration was achieved for the $SrIn_2O_4$: Eu^{3+}phosphor by the simultaneous optimizations of the Eu^{3+} ion concentrations at the Sr^{2+} and In^{3+} sites, respectively.

The non-radiative energy transfer from one Eu^{3+} ion to another Eu^{3+} ion may occur by exchange interaction, radiation reabsorption or electric multipolar interaction. The exchange interaction usually occurs when the donor level has a substantial overlap with the acceptor one. This overlap is responsible for the short critical energy-transfer distances (R_c) less than 0.5 nm [38, 39] and makes a part of forbidden transitions to be allowed one. In the present $Sr_{0.92}In_{1.75}O_4$:$0.33Eu^{3+}$ phosphor, the R_c value was estimated to be 0.817 nm, which reveals that the exchange interaction is not the dominant mechanism for the concentration quenching observed for the present

$Sr_{1-y}In_{1.75}O_4$:(y+0.25)Eu^{3+} phosphors. On the other hand, the radiation reabsorption is only effective when the fluorescence and absorption spectra are broadly overlapping. Since such a broad spectral overlap was not observed for the $Sr_{0.92}In_{1.75}O_4$:0.33Eu^{3+} phosphor as seen in Figs. 4-3 and 4-9 (a), this mechanism can be excluded in the present case. Therefore, the electric multipolar interaction should be the dominant mechanism for concentration quenching of PL emission due to Eu^{3+} ions in the $Sr_{1-y}In_{1.75}O_4$:(y+0.25)Eu^{3+} phosphors.

In this study, the PL red-emitting properties related to the dominant Eu^{3+} occupying site were clarified. Then, for the PL red emission, the optimized total concentration of Eu^{3+} ions which occupied all the Sr^{2+} and In^{3+}sites in the host $SrIn_2O_4$ was determined as 33%, and the Eu^{3+} substitutions in the host $SrIn_2O_4$ can be summarized as follows: The In^{3+} site in the host $SrIn_2O_4$ could be selectively substituted by Eu^{3+} ions by controlling the chemical composition as $SrIn_{(2-x)}O_4$:xEu^{3+} (x: up to approximately 0.3), while it was impossible to replace Sr^{2+} with Eu^{3+} selectively by controlling the chemical composition as $Sr_{(1-x)}In_2O_4$:xEu^{3+}. As a result, $SrIn_{(2-x)}O_4$:xEu^{3+} formed accompanied by the phase separation of In_2O_3. On the other hand, the Sr^{2+} in the $SrIn_{(2-x)}O_4$:xEu^{3+} was found to be replaced with Eu^{3+}, and the Eu^{3+} concentration at the Sr^{2+} site could be increased to 10 % ($Sr_{1-y}In_{1.75}O_4$:(y+0.25)Eu^{3+}, y=0.1). Formation of $SrIn_{(2-x)}O_4$:xEu^{3+} lead to the lattice expansion of the host $SrIn_2O_4$, which was thought to be one of critical factors for the Eu^{3+} substation at the Sr^{2+} site to form $Sr_{(1-y)}In_{(2-x)}O_4$:(x+y)Eu^{3+}.

Finally, to examine the potential for white-LED applications, the temperature dependence of emission intensity under excitation at 393 nm of $Sr_{0.92}In_{1.75}O_4$:0.33Eu^{3+} phosphor was studied. The intensities evaluated up to 500 K (227 ℃) were normalized by that at room temperature and plotted as a function of temperature (Fig. 4-11). The PL intensity decreased slowly with increasing temperature, however the normalized PL intensities at 400 K (127 ℃) and 440 K (167 ℃) remained approximately 90 and 85 %, respectively. Thus, the $Sr_{0.92}In_{1.75}O_4$:0.33Eu^{3+} was found to have a good thermal-quenching property compatible with that of $CaIn_2O_4$:Eu^{3+} phosphor [20] at the usual LED's operating temperatures.

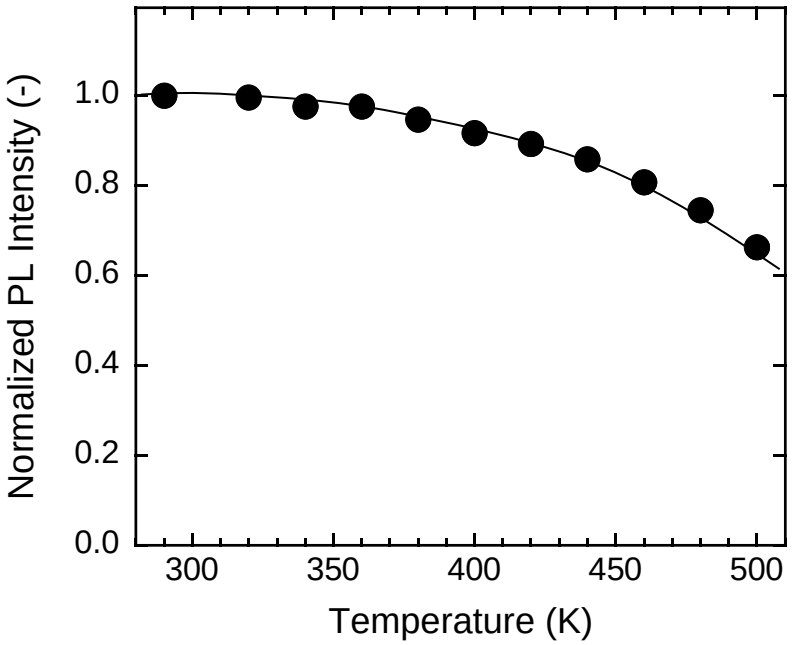

Fig. 4-11. The PL intensity of the $Sr_{0.92}In_{1.75}O_4$:0.33Eu^{3+} under excitation of 393 nm at temperatures from room temperature to 500 K (227 ºC).

4.4. Summary

In this study, $SrIn_2O_4$:Eu^{3+} phosphors were synthesized by the solid solution method at 1400 ℃ in air. To optimize the performance as a red-emitting phosphor for white LED applications, the relation between the Eu^{3+} substitution site and photoluminescence (PL) properties was investigated. The results are summarized as follows:

(1) The dopant Eu^{3+} ions principally occupy two different crystallographic In^{3+} sites, which is thought to be governed by the valence difference between Sr^{2+} and Eu^{3+}, which leads to the intrinsic Eu^{3+} content restriction in the host $SrIn_2O_4$.

(2) Sr^{2+} in the $SrIn_{(2-x)}O_4$:xEu^{3+} was found to be replaced with Eu^{3+}. The lattice expansion induced by the Eu^{3+} substation at the In^{3+} site was thought to be one of critical factors for the $Sr_{(1-y)}In_{(2-x)}O_4$:(x+y)Eu^{3+} formation.

(3) Under excitation of the $^7F_0 \rightarrow {}^5L_6$ transition of Eu^{3+} at 393 nm, the $SrIn_2O_4$:Eu^{3+}

exhibits dominant red emission peaks at 611, 616 and 623 nm, which are attributed to the electric dipole transition $^5D_0 \rightarrow {}^7F_2$ of Eu^{3+}.

(4) The red emission peak intensities at 611, 616 and 623 nm were dominantly governed by the total amount of Eu^{3+} ion at the two different In^{3+} sites, while a small amount (< 10 mol%) of Eu^{3+} ion at Sr^{2+} site was found to contribute to enhance the red emission peak intensity at 616 nm.

(5) The highest red emission intensity evaluated as the total emission peak intensities at the 611, 616 and 623 nm was achieved for 33 mol% Eu^{3+}-doped $SrIn_2O_4$ phosphor in which Eu^{3+} ion concentrations at the In^{3+} and Sr^{2+} sites were simultaneously optimized as 25 and 8 mol%, respectively ($Sr_{0.92}In_{1.75}O_4:0.33Eu^{3+}$). This red emission intensity was 2.2 times higher than that of the phosphor without contribution of the Eu^{3+} at the Sr^{2+} site ($SrIn_{1.75}O_4:0.25Eu^{3+}$).

(6) The oxidation state of the doped Eu ions in the $Sr_{0.92}In_{1.75}O_4:0.33Eu^{3+}$ synthesized in this study was determined as trivalent by the XANES spectroscopic analysis.

(7) The critical energy transfer distance of Eu^{3+} ion in the $Sr_{0.92}In_{1.75}O_4:0.33Eu^{3+}$ phosphor was determined to be 0.817 nm, and the electric multipolar interaction was suggested as the dominant mechanism for concentration quenching observed for the Eu^{3+}-doped $SrIn_2O_4$ phosphor investigated in this study.

(8) $Sr_{0.92}In_{1.75}O_4:0.33Eu^{3+}$ phosphor synthesized in this study exhibited a good thermal-quenching property at the usual LED's operating temperatures.

References

[1] S. Wang, W. Chen, Y. Li, J. Wang, H. Sheu, R. Liu, Neighboring-Cation Substitution Tuning of Photoluminescence by Remote-Controlled Activator in Phosphor Lattice, J. Am. Chem. Soc. 135 (2013) 12504-12507.

[2] M. Tsang, C. Chan, K. Wong, J. Hao, Comparative Studies of Upconversion Luminescence Characteristics and Cell Bioimaging Based on One-Step Synthesized Upconversion Nanoparticles Capped with Different Functional Groups, J. Lumin. 157 (2015) 172-178.

[3] J. Thomas, N. Hans, R. Cees, New Developments in the Field of Luminescent Materials for Lighting and Displays, Angew. Chem. Int. Ed. 37 (1998) 3084-3103.

[4] H. Höppe, Recent Developments in the Field of Inorganic Phosphors, Angew. Chem. Int. Ed. 48 (2009) 3572-3582.

[5] L. Chen, C. Lin, C. Yeh, R. Liu, Light Converting Inorganic Phosphors for White Light-Emitting Diodes, Materials 3 (2010) 2172-2195.

[6] K. Li, X. Liu, Y. Zhang, X. Li, H. Lian, J. Lin, Host-Sensitized Luminescence Properties in $CaNb_2O_6:Ln^{3+}$ ($Ln^{3+}=Eu^{3+}/Tb^{3+}/Dy^{3+}/Sm^{3+}$) Phosphors with Abundant Colors, Inorganic Chemistry 54 (2015) 323-333.

[7] Y. Uchida, T. Taguchi, Lighting Theory and Luminous Characteristics of White Light-Emitting Diodes, Opt. Eng. 44 (2005) 124003-124009.

[8] H. Jang, W. Bin, D. Lee, D. Jeon, S. Kim, Enhancement of Red Spectral Emission Intensity of $Y_3Al_5O_{12}:Ce^{3+}$ Phosphor via Pr Co-Doping and Tb Substitution for the Application to White LEDs, J. Lumin. 126 (2007) 371-377.

[9] G. He, D. Guo, C. He, X. Zhang, X. Zhao, C. Duan, A Color-Tunable Europium Complex Emitting Three Primary Colors and White Light, Angew. Chem. Int. Ed. 48 (2009) 6132-6135.

[10] T. Wang, P. Li, H. Li, Color-Tunable Luminescence of Organoclay-Based Hybrid Materials Showing Potential Applications in White LED and Thermosensors, Appl. Mater. Interfaces 6 (2014) 12915-12921.

[11] J. Park, H. Moon, D. Kim, S. Byeon, B. Kim, K. Suh, Morphology and Cathodoluminescence of Li-doped $Gd_2O_3:Eu^{3+}$, a red phosphor operating at low voltages, App. Phys. Lett. 77 (2000) 2162-2165.

[12] M. Hong, J. Kwo, A. Kortan, J. Mannaerts, A. Sergent, Epitaxial Cubic Gadolinium Oxide as a Dielectric for Gallium Arsenide Passivation, Science 283 (1999) 1897-1900.

[13] C. Rodriguez-Garcia, N. Perea-Lopez, G. Hirata, S. Denbaars, Red-emitting $SrIn_2O_4:Eu^{3+}$ Phosphor Powders for Applications in Solid State White Lamps, J. Phys. D 41 (2008) 092005.

[14] S. Khatkar, S. Han, V. Taxak, G. Sharma, D. Kumar, Synthesis and Luminescence Properties of $CaIn_2O_4$:xTb Nanocrystals, Current Applied Physics 6s1 (2006) e192-e194.

[15] S. Khatkar, S. Han, V. Taxak, G. Sharma, D. Kumar, The Influence of Sintering Temperature on Particle Size/Shape and Photoluminescence Characteristics of $CaIn_2O_4$:xTb Synthesized by Combustion Process, Optical Materials 29 (2007) 1362-1366.

[16] X. Liu, R. Pang, Q. Li, J. Lin, Host-sensitized Luminescence of Dy^{3+}, Pr^{3+}, Tb^{3+} in Polycrystalline $CaIn_2O_4$ for Field Emission Displays, J. Solid State Chem. 180 (2007) 1421-1430.

[17] X. Liu, C. Lin, J. Lin, White Light Emission from Eu^{3+} in $CaIn_2O_4$ Host Lattices, App. Phys. Letts. 90 (2007) 081904.

[18] J. Gou, D. Zhang, B. Yu, J. Wang, S. Liu, The photoluminescence Behaviors of a Novel Reddish Orange Emitting Phosphor $CaIn_2O_4:Sm^{3+}$ Codoped with Zn^{2+} or Al^{3+} Ions, Journal of Nanomaterials 1 (2014) 969724.

[19] X. Liu, C. Li, Z. Quan, Z. Cheng, J. Lin, Tunable Luminescence Properties of $CaIn_2O_4:xEu^{3+}$ Phosphors, J. phys. Chem. C 111 (2007) 16601-16607.

[20] X. Yan, W. Li, K. Sun, A Novel Red Emitting Phosphor $CaIn_2O_4:Eu^{3+}$, Sm^{3+} with a Broadened Near-ultraviolet Absorption Band for Solid-state Lighting, Materials Research Bulletin 46 (2011) 87-91.

[21] F. Kao, T. Chen, A Study on the Luminescent Properties of Red-Emitting

Praseodymium-Activated $SrIn_2O_4$ Phosphors, J. Solid State Chemistry 156 (2001) 84-87.

[22] P. Li, Z. Wang, Z. Yang, Q. Guo, $SrIn_2O_4:Eu^{3+}$, Sm^{3+}: A Red Emitting Phosphor with a Broadened Near-Ultraviolet Absorption Band for Solid-State Lighting, J. Electro. Soc. 158 (2011) 1201-1205.

[23] X. Nguyen, T. Nguyen, V. Chau, M. Dang, The Fabrication of GaN-Based Light Emitting Diodes (LEDs), Adv. Nat. Sci. 1 (2010) 025015.

[24] R. Schenck, H. Buschbaum, Crystal Structure Investigation on $SrIn_2O_4$, Z. Anorg. Allg. Chem. 398 (1973) 24-30.

[25] J. Tang, Z. Zou, J. Ye, Effect of Substituting Sr^{2+} and Ba^{2+} for Ca^{2+} on the Structural Properties and Photocatalytic Behaviors of $CaIn_2O_4$, Chem. Mater. 16 (2004) 1644-1649.

[26] A. Baszczuk, M. Jasiorski, M. Nyk, J. Hanuza, M. Maczka, W. Strek, Luminescence Properties of Europium Activated $SrIn_2O_4$, J. Alloys Compd. 394 (2005) 88-92.

[27] Z. Wang, P. Li, Z. Yang, Q. Guo, Improving Luminescent Property of $SrIn_2O_4:Eu^{3+}$ by Co-Doped A^+ (A=Li, Na, K) or Sm^{3+}, Chin. Phys. B 22 (2013) 047804.

[28] N. Lakshminarasimhan, U. Varadaraju, Role of Crystallite Size on the Photoluminescence Properties of $SrIn_2O_4:Eu^{3+}$ Phosphor Synthesized by Different Methods, J. Solid State Chem. 181 (2008) 2418-2423.

[29] C. Rodríguez-García, N. Perea-López, G. Hirata, S. DenBaars, Red-Emitting $SrIn_2O_4:Eu^{3+}$ Phosphor Powders for Applications in Solid State White Lamps, J. Phys. D 41 (2008) 092005.

[30] S. Dali, V. Sundar, M. Jayachandran, M. Chockalingam, Synthesis and Characterization of AIn_2O_4 Indates, A= Mg, Ca, Sr, Ba, J. Mater. Sci. Lett. 17 (1998) 619-623.

[31] M. Courtney, N. Spellmeyer, H. Jiao, D. Kleppner, Classical, Semiclassical, and Quantum Dynamics in the Lithium Stark System, Phys. Rev. A 51 (1995) 3604-3620.

[32] P. Epstein, The Stark Effect from the Point of View of Schroedinger`s Quantum Theory, Phys. Rev. 28 (1926) 695-710.

[33] M. Aoyama, T. Hayakawa, S. Honda, Y. Iwamoto, Development Zeolite-derived Novel Aluminosilicate Phosphors, J. Lumin. 132 (2012) 2603-2607.

[34] D. Wen, J. Shi, A Novel Narrow-line Red Emitting $Na_2Y_2B_2O_7$:Ce(3+), Tb(3+), Eu(3+) Phosphor with High Efficiency Activated by Terbium Chain for Near-UV White LEDs, J. Dalton Trans. 42 (2013) 16621-16629.

[35] Z. Ju, R. Wei, X. Gao, W. Liu, C. Pang, Red Phosphor $SrWO_4:Eu^{3+}$ for Potential Application in White LED, Opt. Mater. 33 (2011) 909-913.

[36] X. Liu, C. Lin, Y. Luo, J. Lin, Host-Sensitized Luminescence of Dy^{3+}, Pr^{3+}, Tb^{3+} in Polycrystalline $SrIn_2O_4$ for Field Emission Displays, J. Electrochem. Soc. 154 (2007) 21-27.

[37] S. Park, K. Lee, S. Unithrattil, H. Yoon, H. Jang, W. Im, Melilite-Structure $CaYAl_3O_7:Eu^{3+}$ Phosphor: Structural and Optical Characteristics for Near-UV LED-Based White Light, J. Phys. Chem. C, 116 (2012) 26850-26856.

[38] W. Liu, C. Huang, C. Wu, Y. Chiu, Y. Yeh, T. Chen, High Efficiency and High Color Purity Blue-Emitting $NaSrBO_3:Ce^{3+}$ Phosphor for Near-UV Light-Emitting Diodes, J. Mater. Chem. 21 (2011) 6869-6874.

[39] D. Wen. Z. Dong, J. Shi, M. Gong, M. Wu, Standard White-Emitting $Ca_8MgY(PO_4)_7:Eu^{2+}$, Mn^{2+} Phosphor for White-Light-Emitting LEDs, J. Solid State Sci. Technol. 2 (2013) 178-185.

CHAPTER 5: Summary

In this study, luminescence properties of Eu^{3+}-doped oxide phosphors were investigated for their practical use in LEDs and/or VFDs. It was expected to be essential to replace the present commercial sulfide- and oxysulfide-based red phosphors which have some drawbacks such as high sensitivity toward moisture and degradation under electron beam excitation. As chemically stable and environmentally benign host materials, Gd_2O_3 and $SrIn_2O_4$ were selected from rare earth oxides and oxide semiconductors, respectively. To enhance the red emission properties of the Eu^{3+}-doped Gd_2O_3 ($Gd_{2-x}Eu_xO_3$), the effect of Li^+ co-doping on the red emission intensity as well as optimizing the amount of Eu^{3+} doped in the host Gd_2O_3 were intensively studied. On the other hand, Eu^{3+} substitution behaviors at the two different In^{3+} and Sr^{2+} sites were investigated by systematically varying the chemical composition of the $SrIn_2O_4$:Eu^{3+} and XRD analysis combined with PL spectroscopic analysis. Then, the optimized total amount of the Eu^{3+} doped in the host $SrIn_2O_4$ to achieve the maximum PL red emission intensity was experimentally determined.

In Chapters 2 and 3, Li^+ co-doped $Gd_{2-x}Eu_xO_3$ phosphors were synthesized by conventional solid state reaction method and the co-precipitation method at 1200 ^oC in air.

In Chapter 2, 0 to 20 mol% of Li^+ doped cubic $Gd_{1.88}Eu_{0.12}O_3$ powders were synthesized at 1200 ℃ by the solid state reaction method. Under excitation of the charge transfer band of Eu^{3+} at 245 nm, the $Gd_{1.88}Eu_{0.12}O_3$ exhibited a dominant PL red emission peak at 611 nm attributed to the electric dipole transition $^5D_0 \rightarrow {}^7F_2$ of Eu^{3+}. The dominant PL red emission peak intensity increased with Li^+ doping and reached a maximum in the range from 12 to 16 mol%. This intensity was approximately 3 times higher than that of undoped $Gd_{1.88}Eu_{0.12}O_3$. Chemical composition analysis revealed that the Li^+ species was completely evaporated from the samples by the heat treatment up to 1200 ℃, and the resulting Li^+-free cubic $Gd_{1.88}Eu_{0.12}O_3$ materials were found to show enhanced thermal stability with respect to the amount of Li^+ doping. Even after annealing at 1300 ℃ (higher than the

cubic/monoclinic phase transformation temperature of 1250 ℃) for 72 h, the XRD analysis indicated that the relative fraction of the cubic phase in the 12 mol% Li^+-doped sample was as high as 90%. The relationship between the amount of Li^+ doping and the asymmetric ratio evaluated for the PL emission spectrum and PL quantum efficiency of the cubic $Gd_{1.88}Eu_{0.12}O_3$ samples suggested that, in addition to enhanced crystallite growth, the formation of additional oxygen vacancies promoted by Li^+ doping contributed to simultaneous enhancement in the PL red emission intensity and the thermal stability of cubic $Gd_{1.88}Eu_{0.12}O_3$.

In Chapter 3, Li^+-doped cubic $Gd_{1.88}Eu_{0.12}O_3$ phosphors were synthesized at 1200 ^oC in air by co-precipitation and solid state reaction methods. The XRD analysis revealed that, regardless of synthetic method, the average crystallite size for Li^+-free $Gd_{1.88}Eu_{0.12}O_3$ was approximately 400 nm, then increased with the amount of Li^+ and at 20 mol%, reached about 2.3 μm. PL spectroscopic analysis revealed that the dominant red emission peak intensity at 611 nm increased consistently with the amount of Li^+-doping, while CP method was found to be effective in improving the red emission intensity at lower amounts of Li^+-doping from 0 to 8 mol%. CL property was studied by mounting the synthesized phosphor on a VFD operated at an anode voltage of 50 V. The $Gd_{1.88}Eu_{0.12}O_3$ exhibited a similar spectrum with an intense red emission peak at 611 nm, and the highest luminance intensity for the CL red emission was achieved for 8 mol% Li^+-doped $Gd_{1.88}Eu_{0.12}O_3$ synthesized by SS method. The evaluation results of PL and CL properties suggested that, besides the crystallite size of $Gd_{1.88}Eu_{0.12}O_3$, dispersion property of Eu^{3+} ions in the host Gd_2O_3 was an important factor for improving luminescent properties of $Gd_{1.88}Eu_{0.12}O_3$. Moreover, under the present VFD operating condition at the low excitation voltage, it was thought to be essential for improving CL emission intensity to maintain a sufficient surface area of $Gd_{1.88}Eu_{0.12}O_3$.

In Chapter 4, Eu^{3+}-doped $SrIn_2O_4$ phosphors were synthesized by the solid solution method at 1400 ℃ in air. The chemical composition of the phosphors was systematically changed to study the relation between the Eu^{3+} substitution site and photoluminescence (PL) properties. Under excitation of the $^7F_0 \rightarrow {}^5L_6$ transition of

Eu^{3+} at 393 nm, the $SrIn_2O_4:Eu^{3+}$ exhibited dominant red emission peaks at 611, 616 and 623 nm which were assigned to the electric dipole transition $^5D_0 \rightarrow {}^7F_2$ of Eu^{3+}. The results of X-ray diffraction analysis combined with PL spectroscopic analysis revealed that Eu^{3+} ions occupied two different crystallographic In^{3+} sites in the host $SrIn_2O_4$, while it was found to be impossible to substitute Sr^{2+} with Eu^{3+}prior to the Eu^{3+} substitution at the In^{3+} sites in the host $SrIn_2O_4$. The intensity of the red emission peaks increased with the total amount of dopant Eu^{3+} ion at the two In^{3+} sites, and reached a maximum at 25 mol% Eu^{3+}-doping ($SrIn_{2-x}O_4:xEu^{3+}$, x=0.25). Moreover, a small amount (<10 mol%) of Eu^{3+} at the Sr^{2+} site in the $SrIn_{2-x}O_4:xEu^{3+}$ was found to contribute to enhance the red emission peak intensity at 616 nm. As a result, the highest red emission intensity evaluated as the total emission peak intensities at the 611, 616 and 623 nm was achieved for $Sr_{0.92}In_{1.75}O_4:0.33Eu^{3+}$ in which Eu^{3+} ion concentrations at the In^{3+} and Sr^{2+} sites were simultaneously optimized as 25 and 8 mol%, respectively ($Sr_{1-y}In_{2-x}O_4:(x+y)Eu^{3+}$, x=0.25, y=0.08). This red emission intensity was 2.2 times higher than that of the phosphor without contribution of the Eu^{3+} at the Sr^{2+} site ($SrIn_{2-x}O_4:xEu^{3+}$, x=0.25). The critical energy transfer distance of Eu^{3+} ion in the $Sr_{0.92}In_{1.75}O_4:0.33Eu^{3+}$ phosphor was determined to be 0.817 nm, and the electric multipolar interaction was suggested as the dominant mechanism for concentration quenching of PL emission due to Eu^{3+} ions in the Eu^{3+}-doped $SrIn_2O_4$ phosphors.

List of Publication

1. List of publications in this thesis

Chapter 2

(1) "Effect of lithium ion doping on cubic $Gd_{1.88}Eu_{0.12}O_3$: Enhancement of photoluminescence and thermal stability"

Journal of Luminescence, 166 (2015) 238-243.

Yipu Kang[a], Yohei Shimokawa[a], Yasutaka Ishihara[a], Lei Miao[b], Sakae Tanemura[b] and Yuji Iwamoto[a*]

[a]Department of Frontier Materials, Graduate School of Engineering, Nagoya Institute of Technology, Gokiso-cho, Showa-ku, Nagoya, 466-8555, Japan

[b]Key Laboratory for Renewable Energy, Guangzhou Institute of Energy Conversion, Chinese Academy of Sciences, Guangzhou, 510640, China

Chapter 3

(2) "Photoluminescence and cathodoluminescence properties of Li^+ doped $Gd_{1.88}Eu_{0.12}O_3$"

Journal of the Ceramic Society of Japan, 123 (2015) 989-994.

Yipu Kang[1], Yohei Shimokawa[1], Yasutaka Ishihara[1], Hitoshi Tsuji[2], Shinobu Hashimoto[3], Lei Miao[4], Tanemura Sakae[4] and Yuji Iwamoto[1*]

[1] Department of Frontier Materials, Graduate School of Engineering, Nagoya Institute of Technology, Gokiso-cho, Showa-ku, Nagoya, 466-8555, Japan

[2] R&D Department, Noritake Itron Corporation, 670-5 Uchimi, Taiki-cho, Watarai-gun, Mie 519-2736 Japan

[3] Department of Materials Science and Engineering, Graduate School of Engineering, Nagoya Institute of Technology, Gokiso-cho, Showa-ku, Nagoya, 466-8555, Japan

[4] Key Laboratory for Renewable Energy, Guangzhou Institute of Energy Conversion, Chinese Academy of Sciences, Guangzhou, 510640, China

Chapter 4

(3) "Relationship between Eu^{3+} substitution sites and photoluminescence properties of $SrIn_2O_4:Eu^{3+}$ spinel phosphors"

Journal of Luminescence, 169 (2015) 78-85.

Yipu Kang[a], Bui Thuy[a], Yohei Shimokawa[a], Tomokatsu Hayakawa[a], Satoshi Sakaida[a], Lei Miao[b], Sakae Tanemura[b], Sawao Honda[a] and Yuji Iwamoto[a*]

[a]Department of Frontier Materials, Graduate School of Engineering, Nagoya Institute of Technology, Gokiso-cho, Showa-ku, Nagoya, 466-8555, Japan

[b]Key Laboratory for Renewable Energy, Guangzhou Institute of Energy Conversion, Chinese Academy of Sciences, Guangzhou, 510640, China

2. General list of publications

(1) "Effects of environmental factors on the conversion efficiency of solar thermoelectric co-generators comprising parabola trough collectors and thermoelectric modules without evacuated tubular collector"

Energy Conversion and Management, 86 (2014) 944-951.

Chao Li [a,b], Ming Zhang [c], Lei Miao [a], Jianhua Zhou [a], **Yi Pu Kang** [d], C.A.J. Fisher [e], Kaoru Ohno [c], Yang Shen [f],Hong Lin [f]

[a] Key Laboratory for Renewable Energy, Guangzhou Institute of Energy Conversion, Chinese Academy of Sciences, No. 2 Nengyuan Road, Tianhe District, Guangzhou 510640, PR China

[b] Graduate University of Chinese Academy of Sciences, Beijing 100049, PR China

[c] Department of Physics, Graduate School of Engineering, Yokohama National University, Yokohama 240-8501, Japan

[d] Department of Frontier materials, Graduate School of Engineering, Nagoya Institute of Technology, Gokiso-cho, Showa-ku, Nagoya 466-8555, Japan

[e] Japan Fine Ceramics Center, 2-4-1 Mutsuno, Atsuta-ku, Nagoya 456-8587, Japan

[f] State Key Laboratory of New Ceramic and Fine Processing, Tsinghua University, Beijing 100084, PR China

(2) "Experimental performance of a solar thermoelectric cogenerator comprising thermoelectric modules and parabolic trough concentrator without evacuated tube"

Journal of Electronic Materials, 44 (2015) 1972-1983.

L. MIAO,[1] **Y.P. KANG,**[2] C. LI,[3] S. TANEMURA,[1] C.L. WAN,[4] Y. IWAMOTO,[2] Y. SHEN,[5] and H. LIN[5]

1.—Guangxi Key Laboratory of Information Material, Guangxi Collaborative Innovation Center of Structure and Property for New Energy and Materials, School of Material Science and Engineering, Guilin University of Electronic Technology, Guilin 541004, People's Republic of China.

2.—Department of Frontier Materials, Graduate School of Engineering, Nagoya Institute of Technology, Gokiso-cho, Showa-ku, Nagoya 466-8555, Japan.

3.—Key Laboratory of Polarized Materials and Devices, Ministry of Education, East China Normal University, Shanghai 200062, People's Republic of China.

4.—Graduate School of Engineering, Nagoya University, Nagoya 464-8603, Japan.

5.—State Key Laboratory of New Ceramic and Fine Processing, Tsinghua University, Beijing 100084, People's Republic of China.

(3) "Solution-Processed VO_2-SiO_2 Composite Films with Simultaneously Enhanced Luminous Transmittance, Solar Modulation Ability and Anti-Oxidation Property" Scientific Reports, 7000 (2014) 1-11.

Lili Zhao[1,2], Lei Miao[1], Chengyan Liu[1], Chao Li[1], Toru Asaka[3], **Yipu Kang**[3], Yuji Iwamoto[3], Sakae Tanemura[1,4], Hui Gu5 & Huirong Su[6]

[1]Key Laboratory of Renewable Energy, Guangzhou Institute of Energy Conversion, Chinese Academy of Sciences, Guangzhou, 510640, China,

[2]Graduate University of Chinese Academy of Sciences, Beijing, 100049, China,

[3]Department of Frontier Materials, Graduate School of Engineering, Nagoya Institute of Technology, Gokiso-cho, Showa-ku, Nagoya, 466-8555, Japan,

[4]Japan Fine Ceramic Center, 2-4-1 Mutsuno, Atsuta-ku, Nagoya, 456-8587, Japan,

[5]State Key Laboratory of High Performance Ceramics and Superfine Microstructure, Shanghai Institute of Ceramics, Chinese Academy of Sciences, Shanghai, 200050, China,

[6]Genuine Optronics Limited, Shanghai, 200235, China.

List of presentation at international conferences

(1) Luminescence properties and lithium-doped $Gd_{2-x}O_3:Eu_x$

Yipu Kang, Yohei Shimokawa, Yasutaka Ishihara, Sawao Honda, Lei Miao and Yuji Iwamoto

8th China International Conference on High-Performance Ceramics, Cheng Du (China), November 4-7, 2013.

(2) Photo luminescence properties of $Gd_2O_3:Eu^{3+}$ quantum dot

Yipu Kang, Yohei Shimokawa, Lei Miao, Yuji Iwamoto

Phosphor Safari 2014, Kunming (China) November 08-10, 2014.

(3) Enhancement of the luminescence property of Li^+-doped $Gd_{1.88}Eu_{0.12}O_3$

Yipu Kang, Yasutaka Ishihara, Sawao Honda, Lei Miao and Yuji Iwamoto

6th International Workshop on Advanced Ceramics, Nurnberg (Germany), September 28-30, 2014.

Acknowledgements

First and foremost, I would like to express my sincere gratitude to my supervisor, Professor Yuji Iwamoto at Nagoya Institute of Technology (NITech). Without his assistance and dedicated involvement in every step throughout the process, it is impossible for me to gain the fruitful achievements and my graduation thesis would have never been accomplished. I would like to thank you very much for your support and understanding over these past three years.

I also would like to express my sincere gratitude to Associate Professor Tomokatsu Hayakawa and Associate Professor Shinobu Hashimoto for their helpful suggestions and discussions to my research work throughout this thesis at NITech.

I would like to show my gratitude to Research Associate Sawao Honda and Research Associate Yusuke Daiko for their insightful comments and constructive suggestions on my study at NITech. I would like to thank Associate Professor Toru Asaka for teaching me how to use the transmission electron microscopy (TEM).

In the first two years during my doctor course, Dr. Yohei Shimokawa helped me to do my research work at our laboratory and gave me many suggestions not only for improving my work but also for my daily life. Mr. Yasutaka Ishihara, Miss Bui Thi Thuy and Mr. Satoshi Sakaida helped me a lot on the fabrication of the phosphor materials. Their contribution to my research work is obvious throughout this dissertation.

I would like to thank Prof. Sakae Tanemura and Prof. Lei Miao for their kind help. Three years before, they gave me the chance to come to Japan and enter the doctor course at NITech. I am very grateful to Chemical Process Laboratory`s members for their valuable cooperation in my past study, which leading to my present research work in Japan.

Most importantly, none of this could have happened without my family. During my study in the doctor course at NITech, my father passed away. Thank you very much for your financial support. And I hope you can read my doctor thesis in the heaven. I would like to show gratitude to my mother. Especially, these years, you had a very difficult time. Nevertheless, you encouraged me so many times to study with hopes. I will be sure to do something out of gratitude for her in the future.

March 2016

康頎璞

Kang Yipu